Substrate-Independent Nanomaterial Deposition

Via Hypersonic Impaction

by

Peter Firth

A Thesis Presented in Partial Fulfillment
of the Requirements for the Degree
Master of Science

Approved June 2015 by the
Graduate Supervisory Committee:

Zachary Holman, Chair
Michael Kozicki
Michael Goryll

ARIZONA STATE UNIVERSITY

August 2015

ABSTRACT

In the nano-regime many materials exhibit properties that are quite different from their bulk counterparts. These nano-properties have been shown to be useful in a wide range of applications with nanomaterials being used for catalysts, in energy production, as protective coatings, and in medical treatment. While there is no shortage of exciting and novel applications, the world of nanomaterials suffers from a lack of large scale manufacturing techniques. The current methods and equipment used for manufacturing nanomaterials are generally slow, expensive, potentially dangerous, and material specific. The research and widespread use of nanomaterials has undoubtedly been hindered by this lack of appropriate tooling. This work details the effort to create a novel nanomaterial synthesis and deposition platform capable of operating at industrial level rates and reliability.

The tool, referred to as Deppy, deposits material via hypersonic impaction, a two chamber process that takes advantage of compressible fluids operating in the choked flow regime to accelerate particles to up several thousand meters per second before they impact and stick to the substrate. This allows for the energetic separation of the synthesis and deposition processes while still behaving as a continuous flow reactor giving Deppy the unique ability to independently control the particle properties and the deposited film properties. While the ultimate goal is to design a tool capable of producing a broad range of nanomaterial films, this work will showcase Deppy's ability to produce silicon nanoparticle films as a proof of concept.

By adjusting parameters in the upstream chamber the particle composition was varied from completely amorphous to highly crystalline as confirmed by Raman spec-

troscopy. By adjusting parameters in the downstream chamber significant variation of the film's density was achieved. Further it was shown that the system is capable of making these adjustments in each chamber without affecting the operation of the other.

DEDICATION

For all the Firths

In Name and in Spirit

ACKNOWLEDGMENTS

First and foremost, I would like to thank my research advisor Dr. Zak Holman. His contagious passion for this work has convinced me that the frustrations, setbacks, long hours, and late nights are weights worth bearing. His freely available knowledge and guidance have been invaluable resources in getting to this point.
`

I am greatly appreciative to my thesis committee, Dr. Michael Goryll and Dr. Michael Kozicki for their willingness to review, critique and guide my work. Their expertise is highly sought after throughout industry and academia and I am very privileged to have their input.

I am also incredibly thankful to my fellow labmates - Prateek, Joe, and Matt. Their consistent willingness to teach, contribute and critique has made this work far better than I could have achieved on my own.

A piece of this accomplishment also belongs to my friends - Craig, Navi, Justin, Michael, Mark, and Albert. Thank you for the encouragement, support, and never ending good times.

Most importantly I would like to thank my family.

To my sister, Alexandra, whose free spirit and passion for saving the planet reminds me that there is a world beyond the lab and that our work should always focus on making it a better place. Thank you.

To my brother and best friend, William, who spent countless hours helping to edit and format this work. You provide an incredible example of what tenacity and dedication really mean, inspiring me to always push a little harder.

To my fiancé, Christine, who provided me patience, understanding, love and support all while earning her MD. I am so happy to be sharing my life with you, and look forward to all we can accomplish together.

To my mother, Anne, whose presence in my life is a constant source of comfort and optimism. You taught me the meaning of love and selflessness and I will carry that with me for the rest of my life.

To my father, William, whose company I miss every day. You showed me the impact a person with both intellect and compassion can have on this world. Your memory gives me the drive to make a difference.

TABLE OF CONTENTS

LIST OF TABLES

LIST OF FIGURES

xi

1   INTRODUCTION

1.1 Motivation

The properties of a material, whether it be the melting point, the band gap, or its reactivity with other materials, what is observed can be thought of as an average of a large number of quantum effects. As the size of the material is brought into the nano-regime, where a particle may consist of less than 10,000 individual atoms, an average is no longer an accurate representation of its behavior. At this size researchers observe that material properties differ wildly from those of the bulk-material counterparts.

In an increasing number of cases these "nano-properties" have been shown to be useful in applications ranging from energy production to medical treatments. In each of these applications, the nanomaterials are carefully constructed to optimize their perfor-mance with outstanding results. However, synthesizing these materials with the specific structure and properties required by the application is no simple task. At such small sizes the final product is often heavily influenced by random variation in process conditions beyond the control of the scientist. This results in production methods that are slow, ex-pensive, small scale, and heavily material specific. The lack of viable production tech-niques has undoubtedly hindered the widespread use of nanomaterials outside of the la-boratory setting.

This work aims to bridge the gap between laboratory and industrial production through the development of a new tool for nanomaterial synthesis and deposition. This tool, referred to as Deppy, overcomes the shortcomings of current production techniques through a novel design that separates the synthesis and deposition process energetically, while still operating as a continuous flow reactor. As will be described, this allows for the

independent adjustment of the nanoparticle properties and the deposited film properties. Furthermore, the tool is capable of depositing a broad range of nanomaterials onto an even broader range of substrates with minimal modification

While the project at large is committed to developing a tool for general nano-material production, the scope of this work is focused on the production of silicon nano-particles (SNPs). SNPs were chosen as the test case because of the large volume of research available on their production, characterization and the sheer amount of diverse applications within the PV field. It is our hope that this research serves as a solid proof of concept to support further research and funding efforts.

1.2 Overview of This Work

This work will begin with an overview of nanomaterial applications. The primary focus will be on the use of SNPs in PV applications concluding with a brief overview of other promising materials on the research radar. The work will then examine the history of SNP production, summarizing the strengths and weaknesses of each method.

Next, Deppy's construction and principles of operation will be described and its capabilities compared with those of the current technology. When relevant, the subsystems used to support the synthesis and deposition processes will also be described. This work will then look into Deppy's promise as an industrial caliber tool, describing the inner workings of the custom software used to control each of its subsystems.

The work will continue with a brief overview of the relevant characterization methods for SNPs, focusing on Raman Spectroscopy. This will lead to the first set of results, conducted on the first iteration of Deppy's design. The data will be examined in the context of making improvements to the tool's overall performance and compared to post-

modification results. Next a second set of results will be presented showcasing the current abilities of the tool and their influence on further modifications. Finally, the future of research involving Deppy (and its inevitable future versions) will be described.

2   NANOPARTICLE CHARACTERISTICS AND APPLICATIONS

The challenge for new solar technologies is that they must be evaluated not only on their scientific merit, but also on their ability to be brought to market quickly and at a reasonable cost. Silicon Nanoparticles (SNPs) are among a select group of emerging technologies that have shown the potential to meet both of these requirements.

Physically SNPs can be thought of as tiny spheres of silicon with sizes ranging from 2 to 20 nm with structures spanning from purely amorphous to purely crystalline. At such a small size nearly half the atoms lie within one lattice constant of the surface, resulting in a drastic change in the particle behavior [1]. As this work will show, the properties of SNPs are heavily influenced by the size, shape, surface termination and impurity doping.

Those who have worked with silane based Plasma Enhanced Chemical Vapor Deposition (PECVD) processes may be familiar with SNPs; they are often referred to as "silane dust," an undesired byproduct of a non-optimized deposition process. In fact, a lot of the research in this field began with studying the synthesis of SNPs with the ultimate goal of eliminating them **[2]**.

As it turns out, SNPs are more than just dust. Researchers have discovered that SNPs exhibit a number of properties with the potential to improve current PV cell performance. These improvements can be broken down into two categories – carrier generation and performance enhancement.

2.1 Carrier Generation

SNPs exhibit three properties that can aid in carrier generation – a size tunable bandgap, multi-exciton generation, and photoluminescence. The size dependent bandgap

of nanomaterials is a well-documented phenomenon. As shown in Figure 1, the bandgap of SNPs has been shown to range in value from 1.12 eV to 2.75 eV for particles less than 10nm in diameter **[3].**
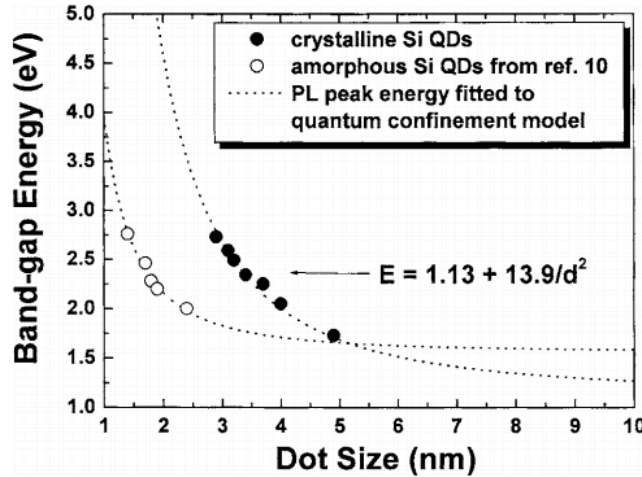
Figure 1 – Bandgap dependence on particle size for SNPs **[3]**

Utilizing this effect with SNPs is of particular promise if researchers are able to accurately control the size and structure. One feasible application would be the construction of a multi-junction solar cell composed of multiple layers of SNPs with varying band gaps. The upper layers composed of high-bandgap SNPs would readily absorb high-energy photons, allowing the lower energy photons to pass through eventually being absorbed by layers of lower bandgap materials [4].

Bulk silicon is an indirect bandgap material. This means that photon emission is facilitated by low probability phonon assisted transitions. Radiative emission must compete with the more favorable non-radiative paths, the result being relatively poor light emission. While using bulk silicon as a light emitter is unlikely, SNPs have been shown to exhibit relatively high photoluminescence quantum yields, in some cases up to 70%.

By controlling the size of synthesized SNPs, and thus the bandgap, through subsequent growth and etching steps, Pi et al. was able to produce particles of a tightly controlled size that emitted light at wavelengths throughout the visible spectrum as shown in the Figure 2 [5]. An application rooted in this result would be the use of an SNP film as a downshifting layer in a standard cell. The SNP film would absorb high-energy photons and then emit lower energy photons that are more efficiently absorbed in the rest of the cell.
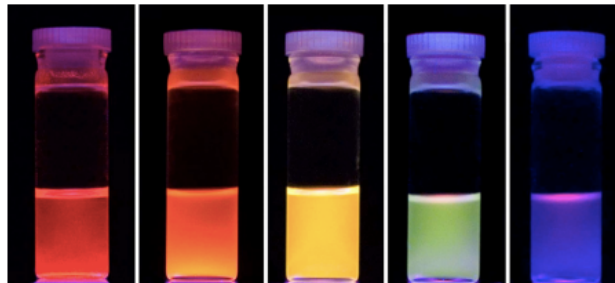
Figure 2 – Light emission from SNPs of varying size excited by a UV lamp [5]
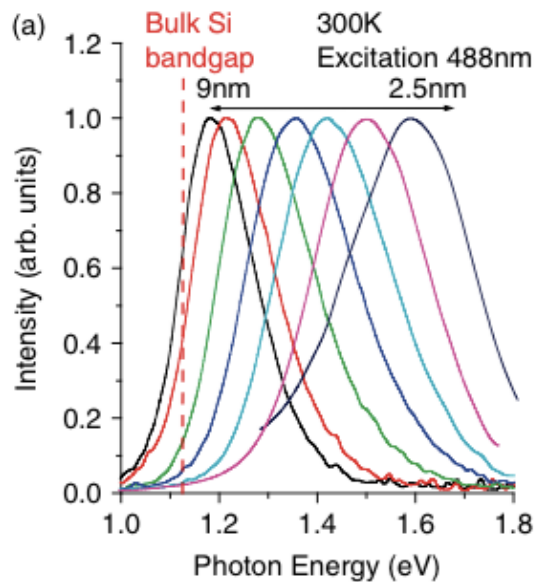
Figure 3 – Optical band gap of SNPs for varying particle diameter **[4]**

Multi-exciton generation (MEG) is a phenomenon describing the generation of multiple electron-hole pairs after the absorption of a single photon with an energy of at least twice the material's bandgap. MEG is one of the holy-grails of PV technology. Of the 67% of solar power unable to be converted to electricity by standard silicon cells, approximately 47% is converted to heat through scattering of hot electrons after absorption of a photon greater than the bandgap. A material that exhibits MEG may prove ideal for capturing this excess energy when used as the cell's absorption layer. Beard et al. was the first to showcase MEG in SNPs, reporting a minimum photon energy of 2.4Eg required to observe the phenomenon and a quantum yield of 2.6 at 3.4Eg. This is a significant improvement when compared to bulk silicon which requires a minimum energy of 3.5Eg to observe MEG [6].

2.2 Performance Enhancement

2.2.1 SNPs for Forming Selective Doped Emitters

While the integration of SNPs into the final structures of next generation solar cells is the focus of a number of research groups, SNPs have already proven useful as an intermediate structure to aid in the selective emitter doping process. The addition of selective emitters is a proven method to increase efficiency in standard cells. They offer a solution to the limitations of a uniformity-doped emitter. A lightly doped emitter allows for a lower saturation current, but results in losses due to poor electrical contact with the metal contact. A heavily doped emitter allows for better electrical contact, but results in an increase in saturation current [7]. Selective emitters eliminate this tug of war by selectively doping the area under the contact more heavily and the bulk of the emitter on the lighter side. Unfortunately, the formation of the two separate doping regions adds extra

processing steps, which often serves as a barrier to implementation. Doped SNPs offer an application method that reduces the number of processing steps, making the selective emitter a more accessible feature.

One method on the market today, a doped silicon ink, was developed by Innovalight (purchased by Du Pont). The manufacture of the ink begins with the synthesis of doped silicon nanoparticles. These are commonly synthesized in a PECVD process with dopant precursors like $POCl_3$, Triethylphosphate, BCl_3 or Triethylborate in addition to silane. The particles are then suspended in a proprietary solvent resulting in a solution with a paste or ink like consistency [8].
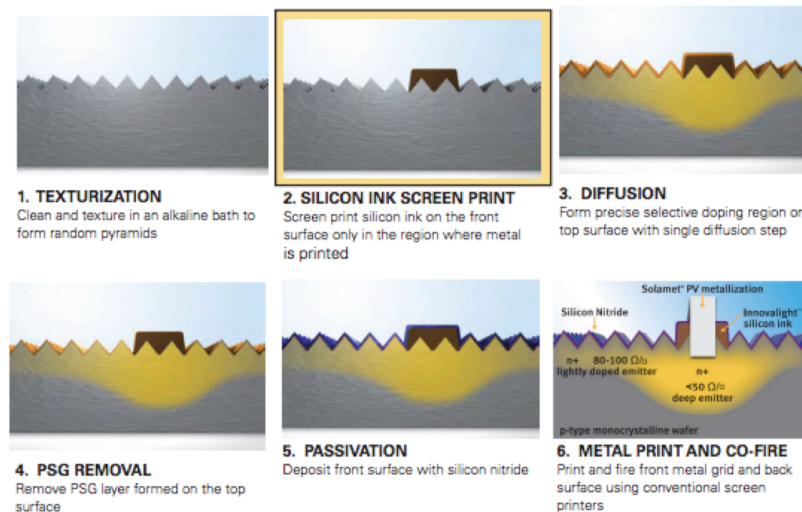
Figure 4 – DuPont's process for forming a lightly doped emitter using a SNP ink [9]

The ink can be used with standard screen printers and printed to` the desired pattern on the substrate. The ink will serve as the localized dopant source for the heavily doped regions, with the doping profile being controlled by the formulation of the ink. After printing, the ink is subjected to a moderately high temperature cycle (~500C) to densify the film. The wafer is then put through a standard diffusion process where gaseous-

dopant precursors are deposited and diffused into the substrate forming the lightly doped regions. In addition to serving as a dopant source for the heavily doped region, the SNP ink acts as a diffusion mask resulting in the formation of two distinctly doped regions.

The application of selective emitters using a SNP ink has been shown to improve cell efficiency by as much as 1% in large scale testing. Given that the use of SNP ink is a non-masking, single step diffusion process, it can easily and inexpensively be integrated into nearly any process flow.

2.2.2 Antireflective Coatings

As their name suggests, anti-reflective coatings (ARC) improve solar cell performance by decreasing the amount of light that is reflected from the surface, increasing the number of photons that reach the active area of the cell [10]. The reflectivity of a substrate/ARC system can be estimated using the following equations:

Equation 1

$$Reflectance = \frac{r_1^2 + r_2^2 + 2r_1r_2cos2\theta}{1 + r_1^2r_2^2 + 2r_1r_2cos2\theta}$$

$$r_1 = \frac{n_0 - n_1}{n_0 + n_1}$$

$$r_2 = \frac{n_1 - n_2}{n_1 + n_2}$$

$$\theta = \frac{2\pi n_1 t_1}{\lambda}$$

Where:
n_o, n_1, n_2 = refractive index of air, the ARC and the substrate, respectively
λ = Wavelength
t = ARC film thickness

Based on Equation 1, the reflectance can be tuned by varying the layer thickness or the refractive index. The refractive index is a material property with a dependence on the material's density. As will be discussed later in this work, the density (and thus the refractive index) of SNP films can be varied by changing the deposition conditions [11]. This will allow for the production of easily tunable ARC films.
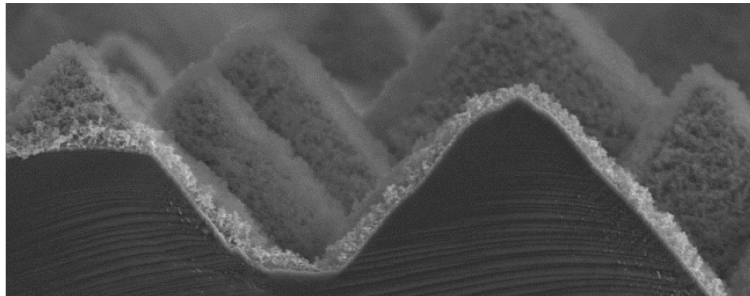
Figure 5 – SNPs deposited on pyramid structures of a solar cell for use as an antireflective coating

2.2.3 Seed Layers for Microcrystalline Silicon Growth

Microcrystalline silicon (uc-Si) is a promising material to replace the doped a-Si layers in heterojunction cells. Its absorption coefficient is much lower than a-Si, meaning more light will reach the cell and the doping efficiency is much higher [11]. uc-Si is typically deposited using a silane and hydrogen based PECVD process. Unfortunately, the growth of microcrystalline silicon is highly substrate dependent [12]. As shown by the Raman spectra in Figure 6, the use of an incompatible substrate results in the deposition of amorphous silicon. This of course limits the potential use of uc-Si to applications that meet the specific underlying layer requirements.
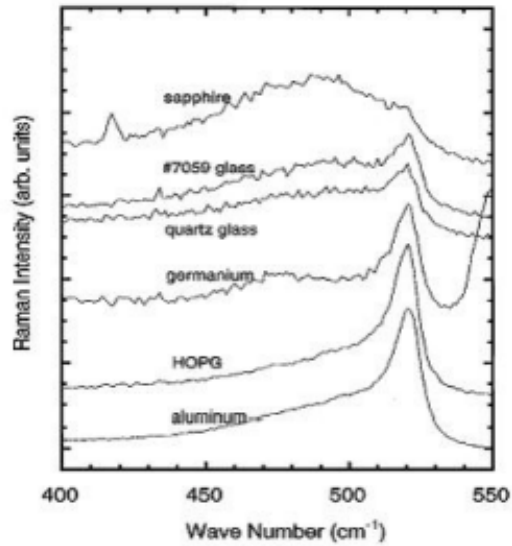
Figure 6 – Raman Spectra for microcrystalline silicon grown on varying substrates. The significant variation implies a significant dependence on the substrate **[**11**]**

The use of randomly oriented crystalline SNPs as a seed layer for uc-Si growth has been shown to reduce the substrate dependence. Taekon Kim of the University of Florida was able to grow crystalline silicon on a SiO2 layer by first depositing a layer of SNPs suspended in a solution. Other groups have also had success using a similar process. Figure 7 shows a clear difference in the film's composition when deposited with and without a SNP seed layer [13].
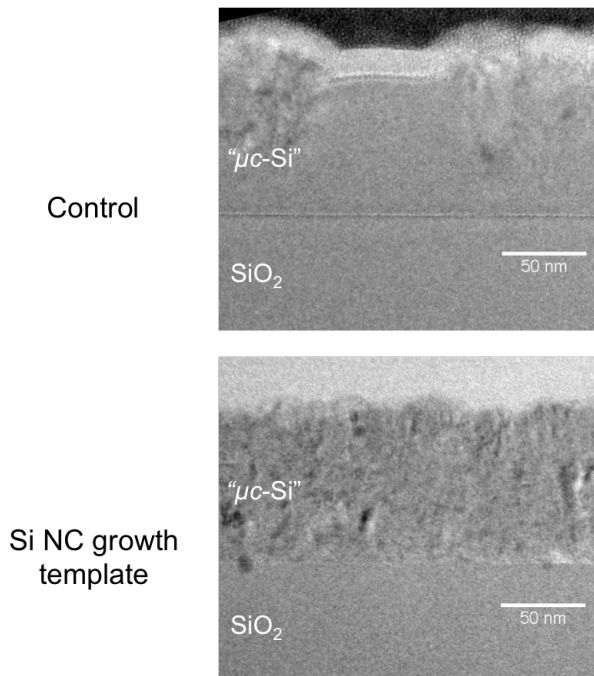
Figure 7 – SEM image showing the effect of an SNP seed layer on the growth of u-cSi. The lower sample deposited with a seed layer clearly exhibits more crystalline properties

2.3 Other Nanomaterials and Their Applications

2.3.1 Platinum

Platinum is used heavily as a catalyst because of its ability to facilitate both oxidation and reduction reactions. It acts as a critical component in catalytic converters, aiding in the conversion of CO into CO_2 and NO_x into N_2 and O_2. Platinum is also key material in hydrogen fuel cells. Since 1998, Platinum has increased in price from \$370/ounce to \$1200/ounce with a peak value of over \$2000/ounce [14]. With over 15 million automobiles sold in the US annually, each equipped with catalytic converter, the market is demanding a method to get more efficiency out of each gram of platinum [15].

A catalysts' efficiency is often tied to its surface area to volume ratio, with a large surface area increasing catalytic activity. But size is not all that matters. The average hydrogen cell on the market today is can produce one ampere per mg of platinum. A group

12

from the University of Copenhagen, headed by Matthias Arenz, was able to improve the conversion efficiency to 8 ampere per mg, by increasing the packing density [16].
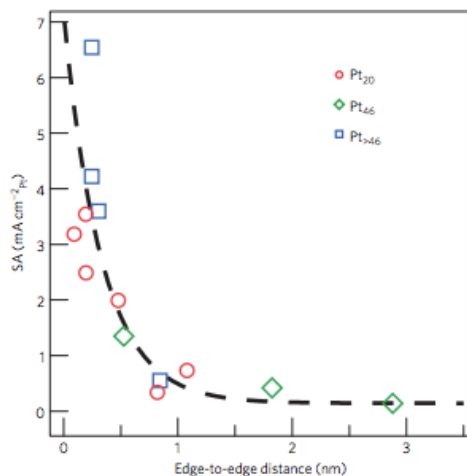
Figure 8 - Oxygen Reduction Reaction (ORR) for three different particle sizes as a function of edge to edge spacing **[16]**

The most common method for production of platinum nanoparticles is the Sol-Gel process. This does allow for control of particle size with a small size distribution, however, the process is slow and the ligands required to dissolve the platinum in the solvent can limit the packing density. There has been some success using plasma based methods. One group has had success by exposing hexafloroplatinic acid (H_2PtCl_6) to a hydrogen plasma. While exciting, this method in its current form is slow and operates as a batch process **[17]**.

3   OVERVIEW OF CURRENT PRODUCTION TECHNOLOGY

While the applications for SNPs and nanomaterials in general are abundant, the synthesis methods and tooling are not. As will be described in the following section, a commonality between each of the methods and tools is their specificity. Not avail- able is a platform capable of producing and depositing multiple materials without heavy modification.

Whether the application is in PV, catalysis, microelectronics or biology, the use of nanomaterials in industrial processes will require the tight control of particle properties (size, composition, surface passivation, etc.), a production rate high enough to not cause a process bottleneck, and the flexibility to produce and deposit a broad range of materials with minimal modification. The following section is an overview of common methods for producing SNPs and other nanomaterials.

3.1 Pyrolysis

One common method used for the synthesis of SNPs is the pyrolysis of silane in a tube furnace. This process can be divided into four sub-processes: particle nucleation, particle growth, the optional surface treatment, and finally deposition onto a substrate. An example of such a system is shown in Figure 9.
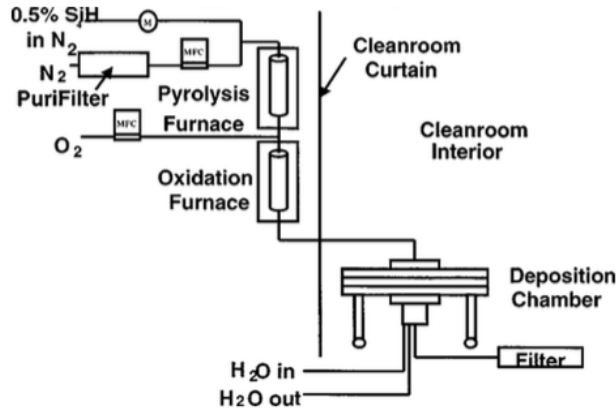
Figure 9 - Three stage SNP pyrolysis system used by Oda [1]

Silane diluted with He or N_2 enters into the pyrolysis furnace. The temperature at the inlet is somewhere in the range of 1000 ^{O}C. Here the silane denatures and particle nucleation occurs. A temperature gradient of 300-500 ^{O}C exists between the inlet and outlet. This increase in temperature facilitates the growth of particles as they travel the length of the furnace. The magnitude of the gradient was found to directly affect the size distribution of collected particles, with smaller gradients resulting in tighter distributions [1].

As the particles exit the pyrolysis furnace, they are often diluted with a carrier gas to inhibit further growth. The particles then enter the surface treatment furnace; in the case of Figure 9 the treatment is a thermal oxidation. Here O_2 gas is introduced and the particles grow a thin oxide shell. Finally the particles leave the surface treatment chamber and enter the deposition chamber where they deposit on the cooled substrate.

While this process may differ slightly from researcher to researcher and application to application, a few generalizations can be made. First particle size has been shown to increase with increased silane concentration and increased residence time. The structure (amorphous vs. crystalline) has been shown to be heavily influenced by residence time, with longer residence times resulting in more crystalline particles [18].

15

One advantage of this method is that the nucleation and growth phases can be easily separated from one another by the introduction of a temperature gradient. This allows individual control over the particle structure and size. This setup is further advantageous because it operates in a continuous flow and is capable of depositing on full size substrates. Further it allows for the collection of individual particles for analysis.

However, this type of setup also brings with it a number of disadvantages. Unfortunately, many gas-phase synthesis methods suffer from uninhibited particle agglomeration, which in a high-temperature environment leads to the formation of a very broad NC size distribution [19]. This method also offers no clear way to control the properties of the deposited film.

3.2 Sol-Gel

One of the most widespread techniques for manufacturing nanomaterials is the sol-gel process. As the name suggests, the sol-gel process results in the formation of a solution dispersed throughout a porous gel. The process begins by introducing a metal, in the form of a metal salt or a metal organic like alkoxide or acetylacetonate, into the appropriate solvent held at a moderate temperature (100 ^{o}C to 300 ^{o}C). Upon mixing, a steep temperature drop will be observed as the solvent aids in the nucleation of the nanoparticles [20].

Depending on the solvent and the temperature, once the nanoparticles reach a certain size they will begin to fall out of solution and form a solid network (the gel). Once the reaction is deemed complete, the solvent must be removed though a drying process that can take anywhere from several hours to several days leaving behind the desired nanoparticles [21].

The sol-gel process has a number of benefits. The surface chemistry of synthe-
sized particles is easily controlled by choosing the appropriate solvent/ligand system. By
properly choosing the solvent, temperature and reaction time, the particle diameters can
also be very accurately controlled with a fairly narrow size distribution, especially for
small particles [22]. Furthermore, it is easy to monitor the average size and size distribu-
tion by monitoring the absorption spectra during the reaction. Figure 10 shows the ab-
sorption spectra of CdSe nanoparticles dispersed in hexane as they grew from 12A in di-
ameter to 115A in diameter. The peak itself corresponds to the average particle size while
the broadness of the peak corresponds to size distribution [23]**.**
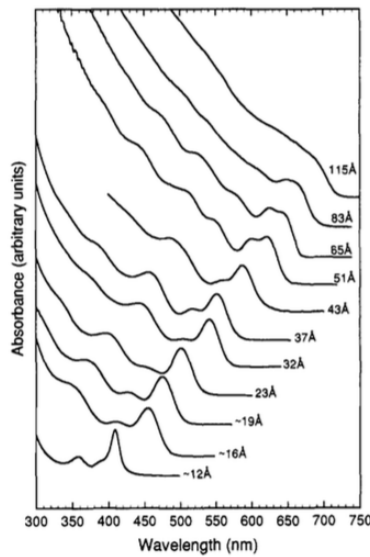
Figure 10 - Average size can be determined by the peak, broadness is representative of
the size distribution. As the size goes up, the peak broadens **[23]**

The sol-gel process is not without its drawbacks. The solvents themselves can be
very expensive and dangerous. The long drying process required to remove the solvents
is often a significant bottleneck. Furthermore, dispersing the particles on a substrate re-
quires the proper solvent selection, which may or may not be ideal for synthesis condi-

tions. This results in a process that requires a very unique protocol for each type of particle and each type of substrate.

3.3 Plasma Generation

The generation of nanomaterials through the use of non-thermal plasmas has become increasingly popular over the course of the last decade, particularly for the synthesis of SNPs. Reactive precursor gasses, generally silane diluted in a carrier gas (He or Ar), are introduced into the plasma chamber where the electrical discharge excites and dissociates the gas. A portion of the dissociated precursor gas gains enough energy through carrier collisions for nucleation to occur. As the nucleated particles flow through the system they continue to grow with a final size proportional to the residence time in the chamber **[**24**]**.

Plasma synthesis of nanomaterials has a number of advantages over previously discussed techniques. First, particle properties can easily be varied by adjusting chamber conditions like applied power, pressure, and gas flowrate [25]. This would likely require a new solvent system in a Sol-Gel process. Plasma processes also offer the opportunity to synthesize multiple types of nanoparticles using the same tool by changing the precursor gasses. Nanoparticles can also be easily doped during synthesis by including gasses like PH_3 and B_2H_6 **[**19**].** Finally plasma processes are easily operated as continuous flow reactors, giving them the ability to produce particles at a much higher rate than Sol-Gel based processes.

However, like the Sol-Gel process, plasma processing is substrate dependent. Furthermore controlling the density of films is very difficult through the electric field alone, producing only "fluffy" non-dense films [25]**.**

3.3.1 ICP Synthesis
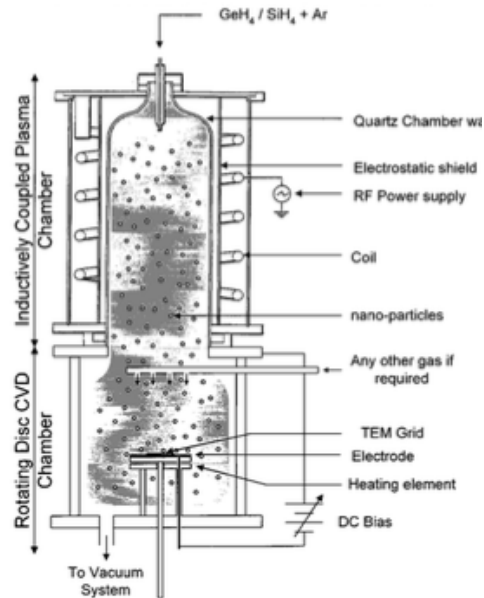
Figure 11 – An inductively coupled plasma SNP sythesis tool developed at Rutgers University

The group of CR Gorla from Rutgers University has had success creating SNPs through the use of a custom Inductively Coupled Plasma (ICP) tool. Gorla's tool consists of a cylindrical quartz tube 20 cm long with a 20 cm diameter wrapped by a RF helical resonator. The substrate sits on a heated chuck reaching temperatures capable of LPCVD with the intent being to incorporate SNPs generated in the plasma into the growing CVD films [26].

The tool operates at pressures of ~200mTorr, powers of 300W to 900W and 1000 sccm of 2% silane in argon. Goral found that increasing the power decreased the particle size, increased the total number of particles and maintained the crystallinity. The group did find however, that if the power was increased above 500W the number of particles significantly decreased. Gorla also found that increasing the silane flowrate increased the average particle size as well as the total particle count. While Gorla's tool is excellent for

19

studying the properties of the particles themselves, it is unable to deposit on full sized substrates. Furthermore, scaling up to incorporate the design into a multi-wafer LPCVD tool may prove to be a significant mechanical challenge.

3.3.2 Pulsed Hydrogen CCP Synthesis

A headed by Oda Shunri has made significant contributions to the understanding of plasma SNP synthesis through their unique "pulsed" plasma tool. The tool is of the Capacitive Coupled Plasma (CCP) category with a total volume of 230 cm^3 operated as a batch reactor. The plasma is formed under ultra-high vacuum conditions with a very high frequency source (144 MHz) and power densities of 0.71 W/cm^2. The purpose of the tool was to control particles size by separating the nucleation and growth phases. Oda accomplished this by developing a "digital" synthesis process, inducing H_2 for a controlled period of time to increase nucleation and limit particle growth.

Using this tool, Oda discovered a number of interesting trends. First, the particle size is proportional to the square root of the gas residence time. It was also found that the addition of H_2 results in a smaller average particle size and an increased particle count. Oda's main contribution however is a process for producing a very narrow size distribution. As shown in Figure 12, by using the pulsed hydrogen technique, Oda achieved an unparalleled size distribution. Many of the principles of the tool's operation, particularly the pulsed H_2 flow, make it an interesting candidate to be scaled up [27].

20
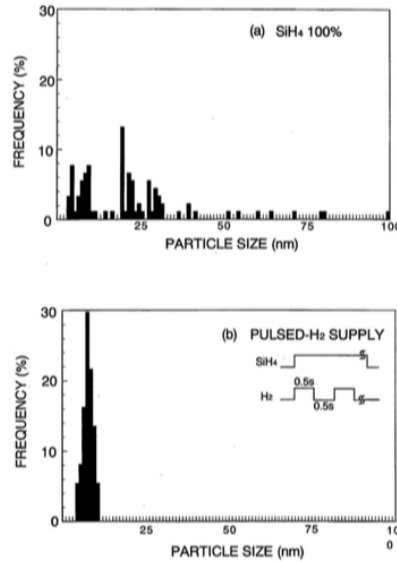
Figure 12 - – Particle size distribution comparison for standard conditions (Top) and pulsed H$_2$ (Bottom) [27]

3.4 Review

Synthesis Method	↑ Particle Size	↑ Crystallinity	↓ Size Distribution	↓ Density
Pyrolysis	↑Residence Time ↑Silane Concentration	↑Residence Time	↓ Temperature Gradient	Limited
Solution Methods	↑Longer processing with heat	Dependent on solvent selections	Dependent on solvent selections	Dependent on solvent selections
Plasma	No Change	↑Power	*Reactor Design *Pulse Hydrogen	Limited

Table 1 – Overview of known methods for controlling nanoparticle properies using popular synthesis techniques

Table 1 summarizes how process conditions influence particle and film properties for each of the methods discussed in the previous section.

From the analysis it is clear that single step (thermal and plasma) tools have the distinct disadvantage of the particle synthesis and film deposition being very tightly coupled. This means that a change in the process parameters designed to vary the film properties will inevitably affect particle synthesis and visa versa. These deposition tools are

21

also very material specific, meaning the same tool cannot be used to deposit both silicon nanoparticles and gold nanoparticles without heavy modification. Multistep processes, like the Sol-Gel process, do decouple synthesis and deposition but face issues with bulk manufacturing, process time, and chemical compatibility.

As the understanding of nanomaterials continues to mature, the focus of research needs to shift from characterization to application. The synthesis methods discussed thus far were developed to produce nanoparticles for analysis and characterization rather than for scalability. The lack of a flexible large-scale production method presents a significant barrier to the implementation of nanomaterial applications.

Based on the analysis above, an industrial grade nanoparticle deposition system should possess the following qualities:

1) Produce a broad range of nanomaterials with minimal modification to the system. Properties of the particles such as size and composition should be controllable

2) Control of film properties like thickness and density

3) Deposit these nanomaterials on substrates of various shapes, sizes and materials

In the sections that follow, this work will show that a new deposition system, referred to as Deppy, meets each of these criteria with its unique ability to separate the synthesis and deposition processes energetically while still operating in a continuous flow.

4   HYPERSONIC PARTICLE DEPOSITION

4.1 Theory of Operation

Hypersonic Particle Deposition (HPD) takes a two-chamber approach to provide continuous nanoparticle synthesis and deposition with independent control of each process. HPD processes are a brute force approach to deposition. Synthesized particles are accelerated to extremely high speeds (up to several km/s) before they impact a substrate like a bullet impacting a solid target. Upon impaction, the particle and substrate deform and adhere to one another via Van der Waals forces [28]. This is a physical process in which the surface chemistry between the particles and substrate plays a small role, allowing for the deposition of a broad range of nanomaterials onto a broad range of substrates with minimal tool and process modification.

In their simplest design, HPD systems consist of three parts: (1) the reaction chamber (RxC), (2) the nozzle, and (3) the deposition chamber (DpC). The RxC is process specific, meaning its design and operation conditions may vary depending on the type of nanoparticles being synthesized. The DpC is a constant design for all types of particle deposition. The two chambers are physically separated by the nozzle, the shape of which varies with the application. Figure 13 below is one of the earliest designs of an HPD tool created by NP Rao of the University of Minnesota.
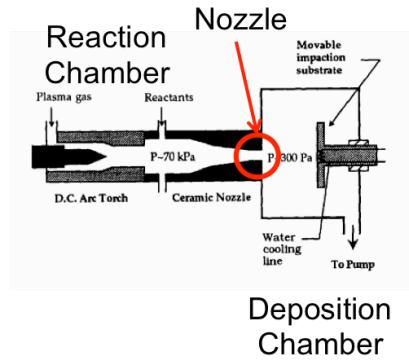
Figure 13 – Early Design of an HPPD System **[28]**

The theory of operation of hypersonic impaction tools can be understood through two primitive thermodynamic concepts, the conservation of energy and the conservation of mass. In fluid mechanics, the conservation of energy is most common-ly represented using the Bernoulli equation [29]**.**

Equation 2 – Full Bernoulli Equation

$$Total\ Energy\ of\ Flowing\ Fluid = \frac{P}{\rho} + U + \frac{v^2}{2} + gz = h + \frac{v^2}{2} + gz$$

Where:

P = Fluid Pressure
ρ = Fluid Density
v = Fluid Velocity
U = Fluid Internal Energy
h = Fluid enthalpy (U + P/ ϱ)
g = Gravitational Constant
z = Height

Assuming the fluid maintains a constant density and temperature (an assumption that will later be revisited) and that changes in height and losses due to friction are negli-gible, the Bernoulli equation reduces to equation 3.

Equation 3 – Simplified Bernoulli Equation

$$Total\ Energy\ (Simplified) = \frac{v_1^2}{2} + \frac{P_1}{\rho} = \frac{v_2^2}{2} + \frac{P_2}{\rho}$$

The first term in the equation is the kinetic energy per unit mass. The second term, the flow energy, represents the energy per unit mass required to move the fluid and maintain the flow [**30**].

Figure 14 represents a gas contained in two large reservoirs connected by a long pipe. If initially both reservoirs start out at the same pressure then $P_1 = P_2$ there will be no net movement of fluid.

Figure 14 – Fluid flow through a constant diameter pipe. The velocity of the fluid will be dependent on the pressure drop as described by the Bernoulli equation

Decreasing the pressure in the second chamber (P_2) results in a decrease in the flow energy. To maintain an overall constant energy in the system, kinetic energy (and therefore velocity) must increase. This results in fluid flow from the high-pressure reservoir to the low-pressure reservoir. Based Bernoulli's equation it is obvious that the greater the pressure differential, the higher the velocity of the fluid will be.
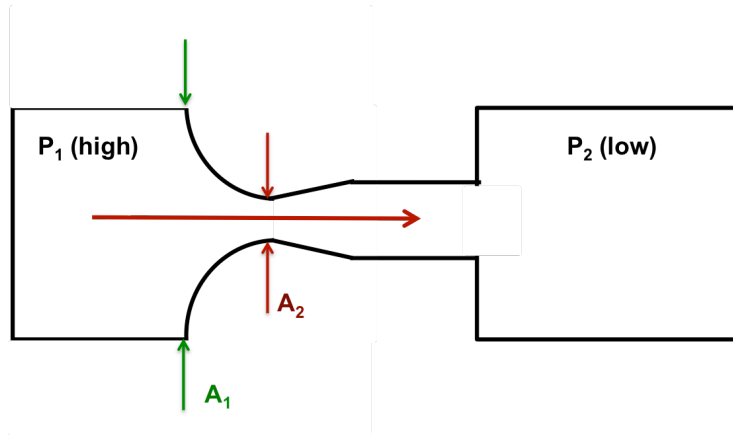
Figure 15 – Fluid flow through a pipe with a restriction. The restriction causes an increase in velocity and a decrease in pressure

Now imagine that this two-reservoir system is further modified so that a restriction in the form of a nozzle exists as shown in Figure 14. When a fluid moves through the restriction it must pass the same amount of mass per unit time through a smaller area. This requires the fluid to increase its velocity, a phenomenon commonly referred to as the Venturi effect. This relationship is described by the continuity equation, Equation 3, below.

Equation 4 – Continuity Equation

$$v_1 A_1 = v_2 A_2$$

Where:
A = Cross-sectional area available for flow

The increase in velocity (kinetic energy) resulting from the fluid passing through the nozzle (where $A_2 < A_1$) must be balanced by a decrease in flow energy. Under the assumption of a constant density and temperature, this energy decrease will come from a decrease in pressure.

In the case of a hypersonic impaction process, it is often desirable to have the gas moving at several km/s in order to maximize the velocity of the dispersed nanomaterial upon impaction. From the above analysis it can be deduced that a fluid's velocity can be increased by both increasing the pressure differential and decreasing the cross-sectional area of the restriction. For a rudimentary tool, this level of understanding may be sufficient, but to more accurately model the fluid flow for industrial uses, the assumption of constant density and temperature must be revisited.

Constant temperature and density of ideal gasses is typically assumed to be accurate for Mach numbers (Ma) less than 0.3. This is shown to be correct through use of Equations 5 and 6. Taking the definition of enthalpy as the product of the specific heat of the fluid and the temperature, the energy balance of a moving fluid slowed down to a stop adiabatically (kinetic energy is completely transferred to flow energy) is described in Equation 5 **[30].**

Equation 5 – Conservation of energy using the definition of enthalpy

$$C_p T_o = C_p T + \frac{v^2}{2}$$

Where:
C_p = Specific heat of the fluid
T_o = Stagnation temperature

Taking,

$$v^2 = c^2 Ma^2 = Ma^2 (\gamma \text{RT})^{1/2}$$

Equation 5 can be rewritten as,

Equation 6 – Temperature dependence on velocity for a compressible fluid

$$\frac{T}{T_0} = \left[1 + \frac{1}{2}(\gamma - 1)Ma^2\right]^{-1}$$

Where:
γ = Specific heat of the fluid

Equation 19 shows temperature's inverse relationship to velocity. At low veloci-ties (Ma<0.3) the change in temperature is minimal, however at high velocities fluid temperature changes can be significant. Using the isentropic flow relations derived from Gibb's equation, equations for the change in pressure and density can also be determined [31].

Equation 7 – Pressure dependence on temperature for a compressible fluid

$$\frac{P}{P_0} = \left(\frac{T}{T_0}\right)^{\gamma/(\gamma-1)}$$

Equation 8 – Density dependence on temperature for a compressible fluid

$$\frac{\rho}{\rho_0} = \left(\frac{T}{T_0}\right)^{1/(\gamma-1)}$$

Using the equations above, it is now possible to accurately plot the parameters of an ideal gas flowing through a restriction as shown in Figure 16 **[32]**.
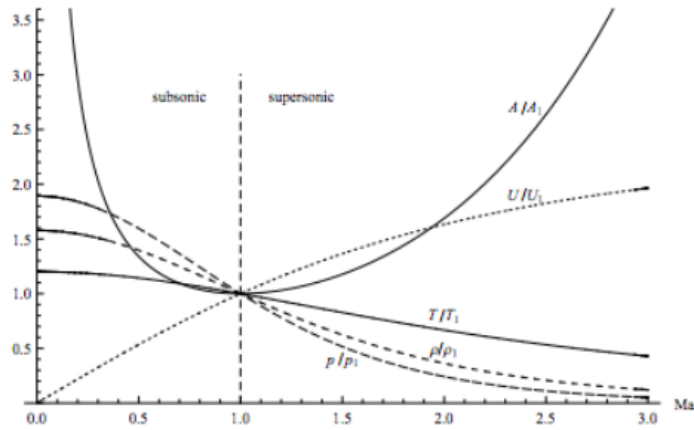
Figure 16- Properties of a compressible fluid forced through a restriction located at x=1 [32]

As the fluid exits the nozzle and enters the lower pressure chamber, it begins to expand to try and match the background conditions, accelerating to velocities several times higher than the speed of sound. As the gas continues to expand its pressure, temperature and density decrease to values below that of the background. The continued acceleration culminates in a near instantaneous adjustment to the background temperature, pressure, density and velocity in a shockwave known as the Mach Disk (MD). The distance the fluid travels into the low-pressure chamber before the MD occurs is determined by Equation 8.

Equation 9 – Distance from the orifice exit that the MD occurs

$$x_m = w \times 1.23 \left(\frac{P_{up}}{P_{down}} \right)^{0.775}$$

Where:

w = Width of an infinitely long nozzle

Figure 17 is an analysis of gas properties after exiting the nozzle at pressure ratios of 40(blue), 20(green), and 10(red) with the inclusion of the MD. As the pressure ratio

29

increases (by decreasing the downstream pressure), the length and maximum velocity of

the jet stream also increases.
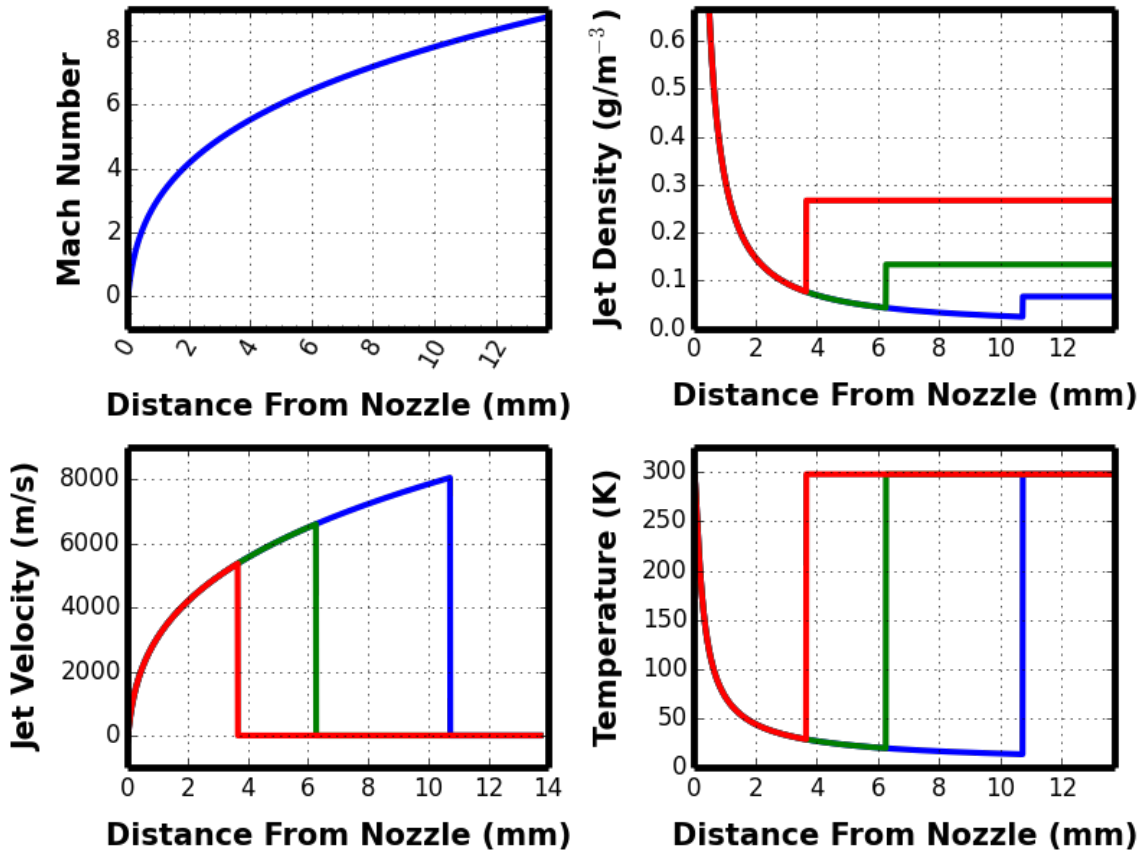
Figure 17- Properties of Helium exiting a restricted opening for pressure ratios of 5(red), 20(green) and 40(blue)

Particles dispersed in the fluid experience a drag force, accelerating them along

the path of the jet stream towards the substrate. For spherical particles less than 30 nm in

diameter, the drag force can be modeled using Equation 9.

Equation 10 – Drag force on a small (<30nm) particle

$$Drag\ Force = \frac{2}{3}d^2\rho\sqrt{\frac{2\pi T}{m}}\cdot\left(1+\frac{\alpha\pi}{8}\right)$$

Where:
ρ = Fluid density

T= Fluid temperature

m = Particle mass

α = accommodation coefficient (a constant specifying the energy transferred between and surface and colliding gas molecule)

Equation 9 shows that the drag force is linearly dependent on the gas density. While the gas density does not affect the length of the jet stream and the location of the MD, it does affect the number of collisions particles experience, with more collisions (higher density) resulting in a larger maximum velocity. Using Equation 9 along with a routine based on the work of Z. Holman and U Kortshagen, the velocity of 5nm diameter silicon nanoparticles dispersed in the fluid is plotted in Figure 18.
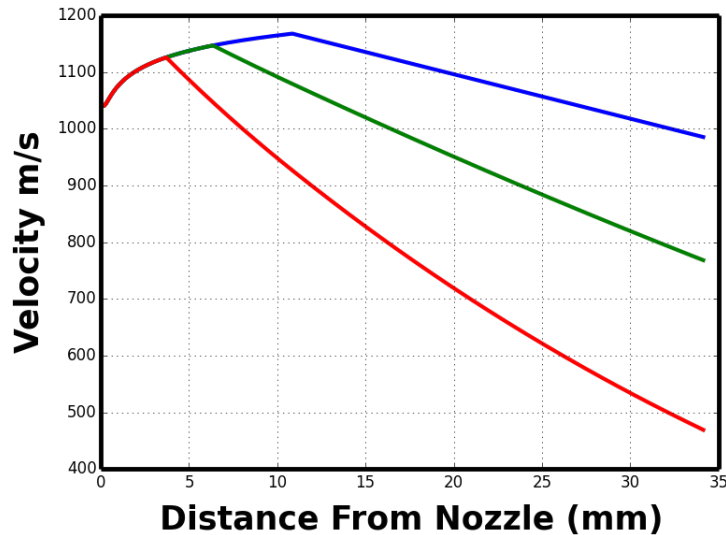
Figure 18- Velocity of a 10nm diameter SNP dispersed in the Helium gas simulated in Figure 17

As shown in Figure 18, the velocity of the nanoparticles can be split into two regimes. In the first regime, the particles accelerate along with the carrier gas, reaching a maximum velocity at the MD. As the jet stream dissociates at the MD and the velocity enters into the second regime, the particles' momentum keeps them moving in the same direction towards the substrate. However collisions with the stagnant background gas

31

begin to slow the velocity down. By placing the substrate at different distances from the nozzle, the impact velocity of the particles can be controlled.

4.2 Deppy

The principles of HPD described in the previous section were used in the development of Deppy, the Holman Lab's custom designed large scale HPD system. The design was heavily influenced by system pioneered by Z Holman and U Kortshagen at the University of Minnesota.
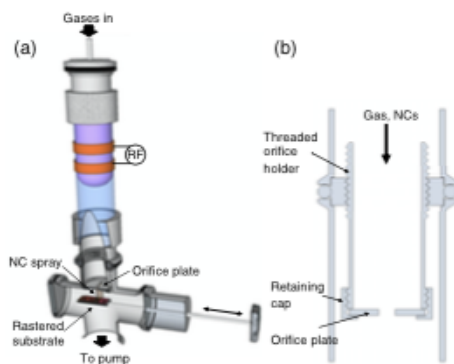
Figure 19– The Holman and Kortshagen small scale HPD system developed at the University of Minnesota [25]

Deppy aims to decouple the synthesis and deposition processes while maintaining the high throughput and the simplicity of single step processing. It is the first HPD system capable of depositing films onto full sized substrates (up to 100mm) and was designed with the capability to deposit multiple types of nanoparticles onto substrates of varying shapes, sizes, and materials.
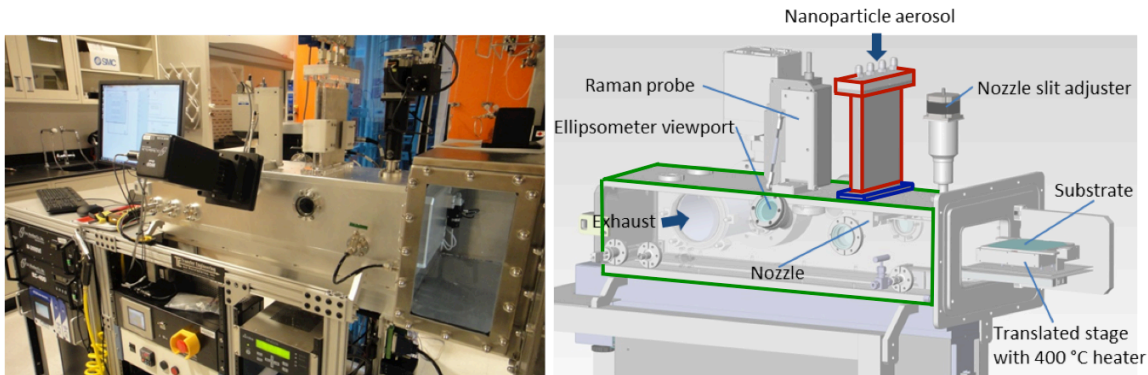
Figure 20 – Arizona State University's large scale HPD system, Deppy

Like other HPD systems, Deppy consists of the three primary sections shown in Figure 20, the RxC (red), the nozzle (blue) and the DpC (green). Precursor gasses are introduced to the reaction chamber where the nanoparticles are formed/modified. The details of the chemistry that occurs in the RxC is material specific. For this reason Deppy's RxC was designed to be easily and inexpensively removed and replaced to fit the specific application.

After passing through the RxC, the nanoparticles are accelerated through the nozzle and into the DpC where they impact a substrate that passes beneath the jet stream, forming a uniform film of nanoparticles. The velocity of the nanoparticles at upon impaction is dependent on the RxC and DpC pressure ratio and the nozzle width. Deppy is equipped to accurately control both these properties via a MKS pressure control valve and the variable width nozzle shown in Figure 21.
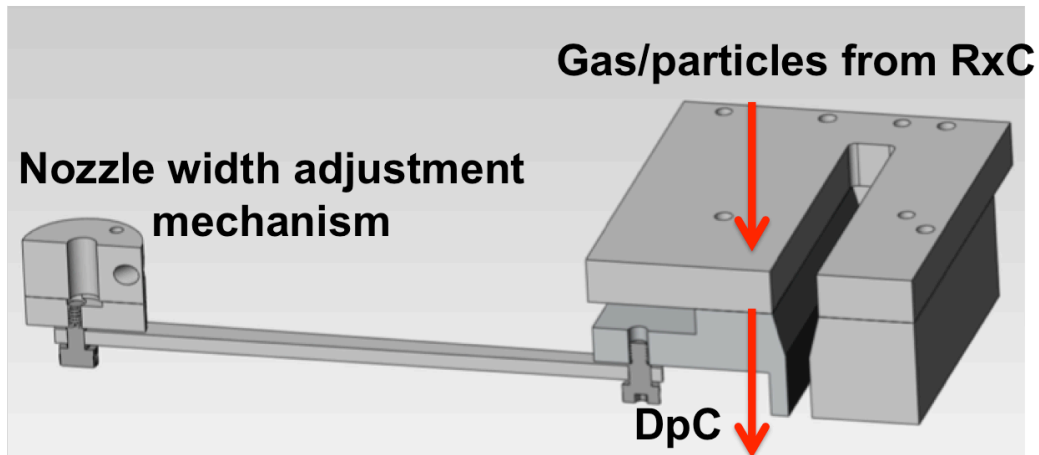
Figure 21 – Cross-section of the variable width nozzle used with Depp

Key Features:

- Deposit on up to 100 mm substrates
- "Swappable" Reaction Chamber
- Reaction Chamber Pressure Range: 50 mTorr to 6000 mTorr
- Deposition Chamber Pressure Range: 50 mTorr to 2000 mTorr
- Substrate X-Velocity: 10 mm/s to 150 mm/s
- Substrate Y-Range: 30 cm

In the sections that follow the critical components that contribute to Deppy's operation will be discussed in detail.

4.2.1 Reaction Chamber Design

The properties of semiconductor nanoparticles formed in non-thermal plasmas have been shown to be dependent on process conditions including applied RF power, chamber pressure and precursor gas flowrate [25]. Therefore, a RxC design should incorporate methods for varying each of these parameters.

The inlet of the chamber is attached via stainless steel gas lines to three mass flow controllers (MFCs) allowing for the introduction of precursor gasses (SiH_4, He, and SiH_4). Within the RxC a plasma is formed (either a ICP or a CCP) through the use of an

RF generator and matching network to provide the energy required for particle nucleation and growth. The RxC lies in series with the DpC and therefore the pressure in the RxC is controlled by varying the width of the nozzle separating the chambers.
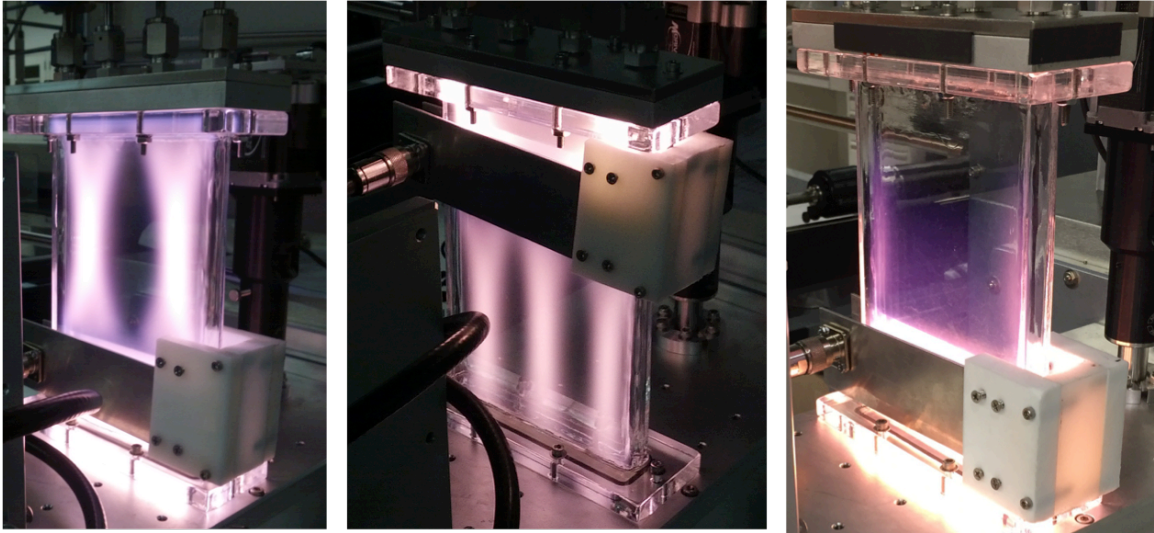
Figure 22- Visible inconsistancy of plasma formation using a quartz reaction chamber

Deppy's initial design utilized a quartz tube as the reaction chamber. While the quartz proved adequate for initial experimentation, its use had a number of drawbacks. In most CCP systems used in industry, the active and ground electrodes are on the inside of the vacuum chamber in direct contact with the gas. With the electrodes on the outside, it was found that the plasma in Deppy's system was not coupling with the ground electrode (removing the electrode from the system did not change the plasma properties) but rather with the showerhead or the DpC body. While coupling with either of those features is not an inherent problem, there was no control over which one occurred on any given run. This resulted in different particle properties for the same input parameters. Figure 22 shows the obvious visual variation in plasma formation under similar conditions with the quartz chamber.

Furthermore, on two separate occasions the quartz body shattered due to either thermal or mechanical stress. This not only resulted in tool downtime, but also raised safety concerns if the tube were to shatter in the middle of a process.
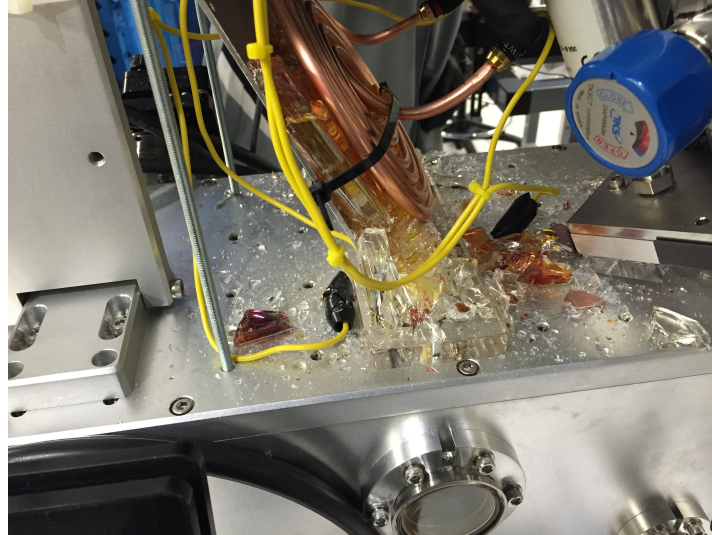
Figure 23- Catestrophic failure of quartz reaction chamber under constant stress

The current design is an aluminum body of the same internal volume (273 cm^3) and shape as the quartz tube. The chamber's two electrodes are electrically isolated from the grounded chamber via a Teflon cover and are in direct contact with the precursor gas. Aluminum was chosen as a material because of mechanical strength, relatively easy machinability and its widespread and proven use in the semiconductor industry.

The chamber was designed to be capable of operating as both a symmetric and asymmetric reactor. Symmetric plasma reactors have hot and ground electrodes that are comparable in surface area and are known to produce very uniform plasmas. The drawback, however, is that the plasma potential in symmetric reactors is very high, the resulting ion bombardment of the electrodes can result in sputtering of undesired material.

36

Asymmetric reactors (one electrode is significantly larger than the other) have a much lower plasma potential, but are inherently non-uniform.
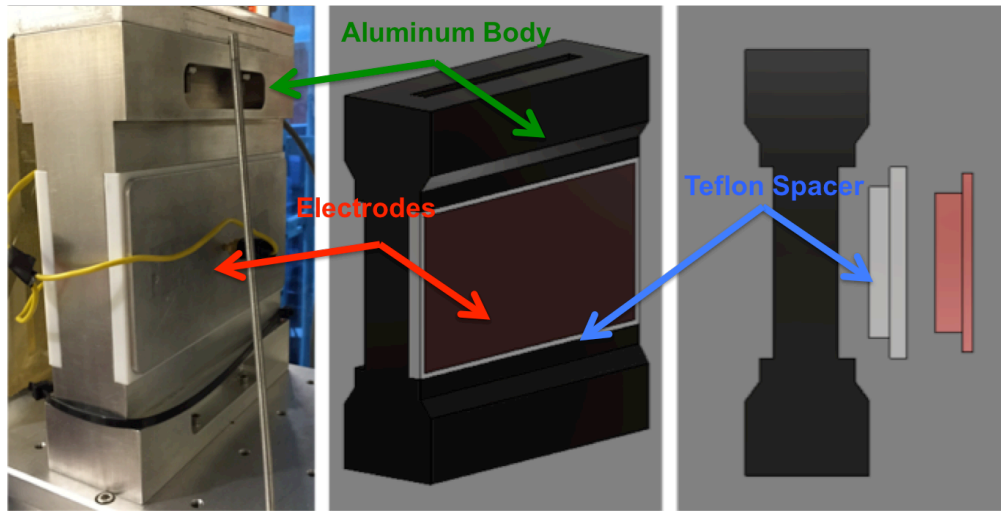
Figure 24 – Aluminum reaction chamber designed to handle rugged opperating conditions

Initial results have proven the aluminum chamber design to be a vast improvement over the quartz. This further proves the advantages of Deppy's design. Because of the compartmentalization Deppy was significantly improved through a $1500 RxC rather than the $200,000 it would have cost to fabricate a new tool.

4.2.2 Deposition Chamber Design

The deposition chamber controls the properties of the nanoparticle films by adjusting the particle's impact velocity (to control density) and substrate's exposure time (film thickness).
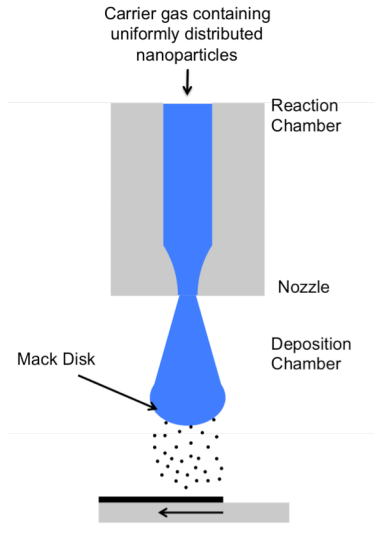
Figure 25 – Visualization of particle flow in the deposition chamber

As indicated by Equation 9, the deposition chamber has three methods by which it is able to adjust the density.

1) Varying the RxC to DpC pressure ratio

    - Accomplished through the use of a MKS butterfly valve. In its current state the valve is capable of controlling pressure from 10mTorr to 2000mTorr with 5mTorr accuracy.

2) Varying the Nozzle width

    - Nozzle width is varied between 0mm and 5mm using a stepper motor capable of varying the nozzle in 0.002mm increments

3) Varying the distance from the nozzle to the substrate

    - Gears couple a stepper motor's movement to vary the distance of the substrate to the nozzle in 0.05mm increments and a total variation of 300mm

As shown in Figure 25, nanoparticles are deposited on a substrate as it passes beneath the jet stream. The thickness of the film after a single pass is dependent on the rate of nanoparticle production (determined upstream in the RxC) and the speed at which the

38

substrate is moving. The substrate speed is controlled via stepper motor and can be varied from 20mm/s to 150 mm/s.

4.2.3 Matching Network Design

A plasma is sustained in a closed loop circuit by flowing current from the generator into the plasma through the chamber walls and back to the generator. In order to optimize power transfer into the plasma it is necessary to match the impedance of the generator to that of the load (chamber + plasma) [33].

An equivalent circuit for a reaction chamber and plasma consists of two capacitive elements and a resistive element arranged in parallel. A properly designed matching network aims to convert the impedance of the chamber and plasma to look like the 50 ohm impedance of the RF power supply and the connecting cables.
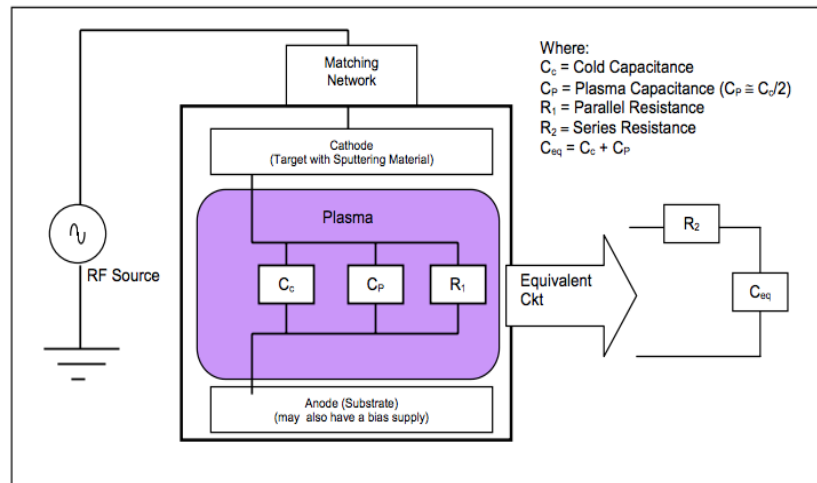
Figure 26 – Equivalent circuit of a capacitively coupled plasma [34]

Within a matching network, the real part of the impedance should be equal to the real part of the load and the reactance should be equal in magnitude but opposite in sign. There are a number of common circuits used for impedance matching in plasma applications with the simplest to implement being the L-Circuit [35].
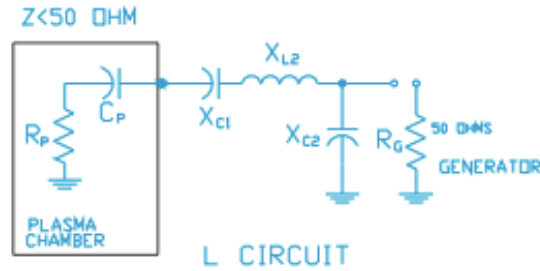
Figure 27 – Typical L-Circuit used in CCP matching networks **[34]**

As shown in the circuit diagram above, an L-Circuit consists of two variable capacitors and an inductor. Since only two components are variable, as apposed to three in the other common circuits, control and automation of L-Circuits are inherently simpler.
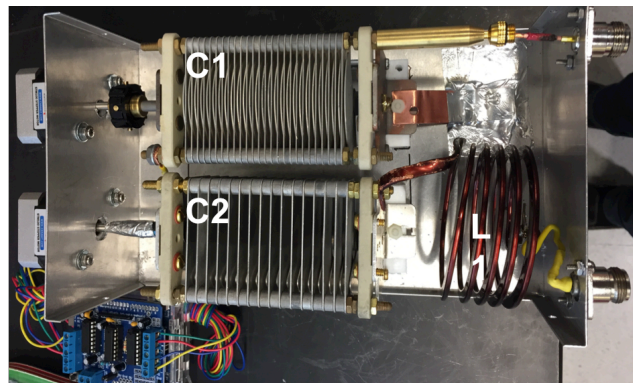
Figure 28 – Matching network designed and built at ASU for use with Deppy

The design of Deppy's matching network was a challenging process since equipment for measuring the cold and plasma capacitance was not readily available. The ultimately successful design strategy was to estimate the chamber's properties and use variable components with a large enough range to account for inaccuracies.

The cold capacitance was calculated assuming the chamber could be modeled as a parallel plate capacitor with helium serving as the dielectric. The plasma capacitance was taken as half of the cold capacitance [39]. This resulted in a reactance at 13.56 MHz of

106 ohms (a reasonable value). The resistive element of the plasma was assumed to be approximately 5 ohms [40].

Using a smith chart, it was determined that the C1 capacitor would require a value of approximately 0.7 nF and the inductor would require a value of approximately 1 nH. A variable capacitor with a range of 0.4 nF to 1 nF was used in the final design for the C1 capacitor. An air-core inductor with an inductance of approximately 3.5 nH was placed in series with a variable capacitor (C2) with a range of 0.3 nF to 0.6 nF. The matching network designed and built for Deppy can be seen in Figure 28. The capacitors are varied using two 1.8o stepper motors controlled using an Arduino Uno and is capable of matching up to 300W (generator limit) with no reflected power.
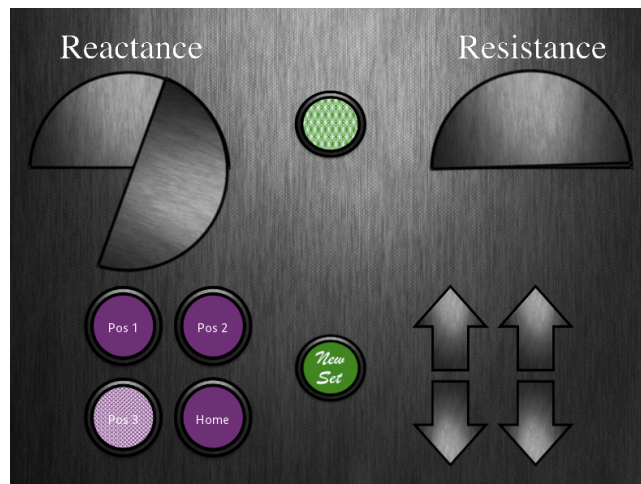
Figure 29 – Software used to interact with the matching network

The software designed for interacting with the matching network is shown in Figure 29. The Arduino keeps track of each capacitor's position and feeds back that information to the computer where it is displayed visually. The capacitors' position can be changed in one of three ways. For large movements, the user can click and drag the capacitor on the screen, this will send the new position to the Arduino which will calculate

the appropriate number of steps to move the motor. For finer adjustments, the up and down toggle buttons can be pressed which move the motors one step clockwise or counter clockwise, respectively. Once the plasma is tuned to the user's satisfaction, the position of the capacitors can be saved to one of four presets. When one of the preset buttons is pressed, the capacitors move to that position for fast and accurate tuning.

4.2.4 Control Software
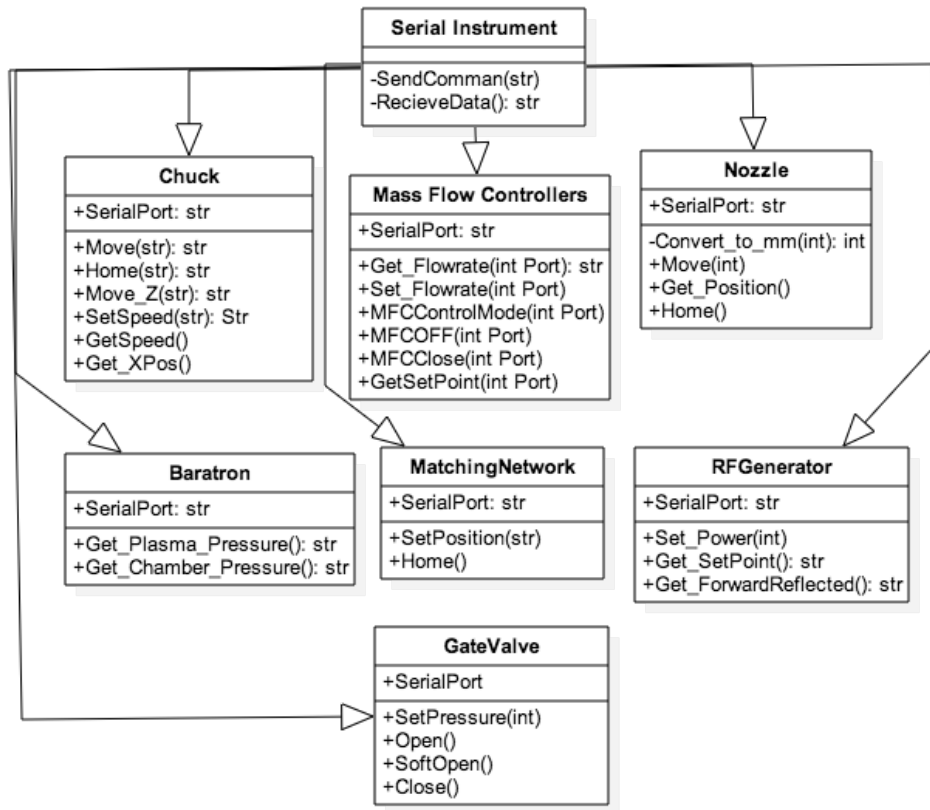
Figure 30 – Unified Modeling Language (UML) diagram of Deppy's control software

Meeting the process specifications and achieving the performance consistency essential for large scale operation requires a deep understanding of the underlying physical phenomenon as well as the ability to control it. There are seven subsystems within Deppy whose synchronized feedback and interactions are key to its successful operation. As an

42

industrial grade system, this synchronization must be automated to the extent that an employee at the operator level can safely and successfully operate the tool. With this philosophy in mind, a considerable amount of time, effort, and consideration was put into the software design.

The software in its current form is written in Python 2.7 using the Kivy framework for graphics support. Python and Kivy were chosen largely for their portability and readability. While LabView and C++ are generally the standards when it comes to equipment automation, we had to consider that in our academic setting future students without extensive programming knowledge may need to interact with the tool. As mentioned, code written in python can be easily understood by novice to intermediate programmers and has an extensive and active community for support.

Figure 30 is the UML (Unified Modeling Language) diagram for Deppy's control system. As shown in the figure, interaction with the subsystems is controlled by the parent class, Serial Instrument. Serial Instrument contains the methods for sending and receiving information via RS-232 protocols. Each subsystem is represented by its own child class and has the necessary methods for forming and parsing the data sent to and from the subsystems.

Safety was a primary concern when designing the software. For a number of nanoparticle synthesis methods, the precursor chemicals can be very dangerous if the tool-operator is exposed. The software is designed so that dangerous materials cannot be introduced into the system until all safety conditions are met (doors closed, chamber under vacuum, vacuum pump on, etc.) and will immediately adjust operations if a safety error is thrown during operation.
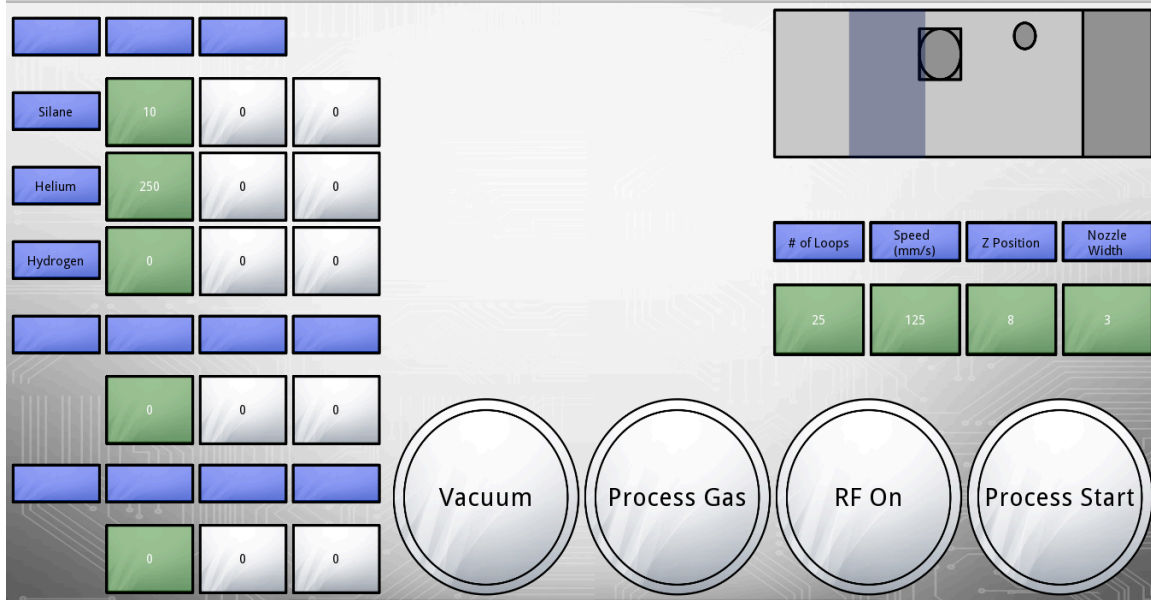
Figure 31 – The interface used to interact Deppy and control its components build using python

Within the GUI (Graphical User Interface) a very high priority was placed on strong and obvious visual feedback. For example, equipment that is currently active in a control mode shows up as a green symbol within the GUI. If the logic senses that a parameter is out of specification, this symbol turns red, alerting the operator to a potential problem with the process. The GUI and the subsystem classes are tied together in the Main method where the communication with each device occurs within its own thread for synchronic operation.

General Operation Procedure

1) Load sample onto the chuck

2) Send the chuck to the home position by pressing the *home* button

3) Close the doors/valves (currently a manual process)

4) Press the *Vacuum* button to bring the tool under vacuum
   - This will trigger a soft pump routine, bringing the tool to vacuum at a controlled rate

5) Set process parameters
   - Power
   - Pressure
   - Gas Flowrate
   - Chuck Speed

6) After two minutes under vacuum, turn on the gasses
   - Gasses will not turn on if the tool is not under vacuum

7) After the pressure has stabilized, turn on the RF power

8) Let the pressure stabilize and start the chucks movement routine

9) When the process is complete, the RF power and gas flow are automatically turned off

10) Bring the chamber to atmosphere and unload the sample (currently a manual process)

In its current state, the software's interaction with the equipment is highly functional and reliable. Working from this basic functionality, we intend to continually add features to make the tool and software more industrially relevant. Currently, we are developing a data logging feature to track process conditions throughout a deposition, a remote monitoring system to alert the tool owner of potential problems and tablet support for maintenance technicians who need access to control features while working in spaces without access to the main computer.

5   RAMAN SPECTROSCOPY

5.1 Overview

The scattering of light can take two forms. The first form is elastic scattering, also known as Rayleigh scattering. In Rayleigh scattering the scattered light has the same wavelength as the incident light. Inelastic scattering, referred to as Raman scattering results in scattered light with a different wavelength than that of the incident light. Raman scattering only occurs in a very small fraction, 1 in 107, of the total scattered light [36].

Raman scattering results from the interaction of photons with the vibrational motion of atoms. Through this interaction, energy is either gained or lost resulting in the characteristic shift in wavelength. The magnitude of this shift is related to the type of bond the photon interacted with and thus analysis of this shift can give information about the material's composition.
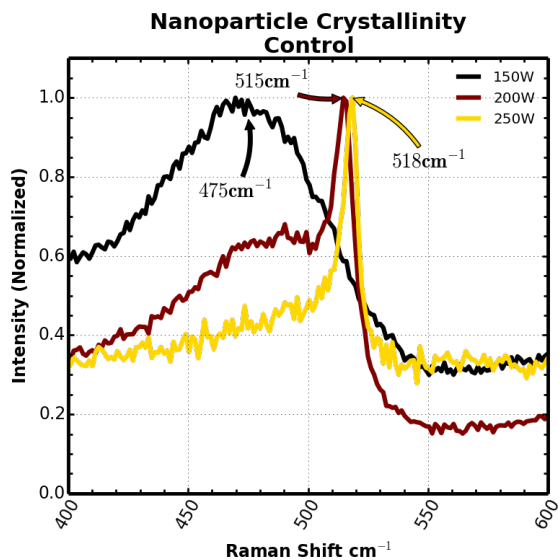
Figure 32 – Raman spectra depicting the three regimes of SNP particle morphology, crystalline (yellow), amorphous (black) and mixed (maroon)

Figure 32 shows the characteristic Raman spectra for a range of SNP structures. The black curve represents an amorphous structure. Raman signals from amorphous silicon are very broad, spanning from ~410 cm^{-1} to ~510 cm^{-1} with a peak at approximately 475 cm^{-1}. The yellow peak represents a highly crystalline structure with a single narrow peak at ~518 cm^{-1}. The Maroon Peak represents a structure between the two, exhibiting signals from both structures.
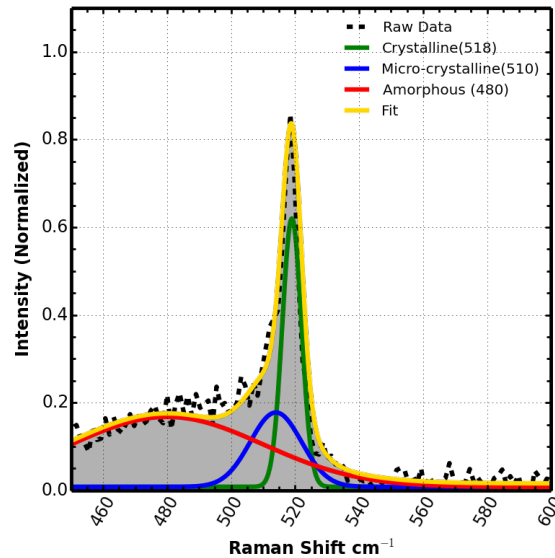
Figure 33 – Deconvolution of a Raman spectra showing the contributions from the crystalline (green), microcrystalline (blue) and amorphous (red) phases

Analysis of Raman spectra requires a method to quantitatively determine the sample's structure. This is commonly accomplished through deconvolution as shown in Figure 33. The data from the Raman spectra is fit through the sum of three Gaussian curves, the parameters of which have a physical meaning. The equation for a normal Gaussian curve is of the form shown in Equation 11.

47

Equation 11

$$f(x) = \frac{a}{c\sqrt{2\pi}} \cdot exp\left(-\frac{(x-b)^2}{2c^2}\right)$$

Where:
a = Influences the height of the curve
b = Position of the peak
c = Influences the width of the curve

Each curve represents the presence a specific material. The green peak at ~518 cm^{-1} is representative of the crystalline phase, the blue peak at ~510 cm^{-1} is representative of the microcrystalline phase and the red peak at ~475 cm^{-1} is representative of the amorphous phase. The area underneath each individual curve can be correlated to the relative percentage of that type of material in the sample. For the purposes of this work, the percentage of crystalline material, the crystallinity, was calculated using the following equation:

Equation 12

$$Crystallinity = \frac{Blue\ Curve\ Area + Green\ Curve\ Area}{Blue\ Curve\ Area + Red\ Curve\ Area + Green\ Curve\ Area}$$

Generally, the three characteristic Gaussian curves are fit to the spectra simultaneously using a least squares (or similar) routine. Early on in this research it was found that fitting the curves simultaneously rarely produces unique fits and is highly dependent on the initial conditions. This can be problematic when attempting to compare data with others. To standardize the process a custom fitting routine was developed specifically for extracting the crystallinity from SNP samples. The routine uses a unique subtraction method to yield consistent and accurate results. The routine operates in the following manner (shown graphically in Figure 34):

1) An amorphous sample (blue curve) and a sample to be fit (purple curve) are taken as inputs.

2) The amorphous curve is scaled down (via multiplication by a scaling factor) until it intersects the three anchor points on the sample. The outer anchor points represent the limits for amorphous silicon's Raman shift and the center point represents the peak

3) The data from the blue curve is subtracted from the purple curve yielding the green curve. The green curve represents the shift caused by *only* crystalline material

4) The blue curve and the green curve are fit separately using a least squares routine
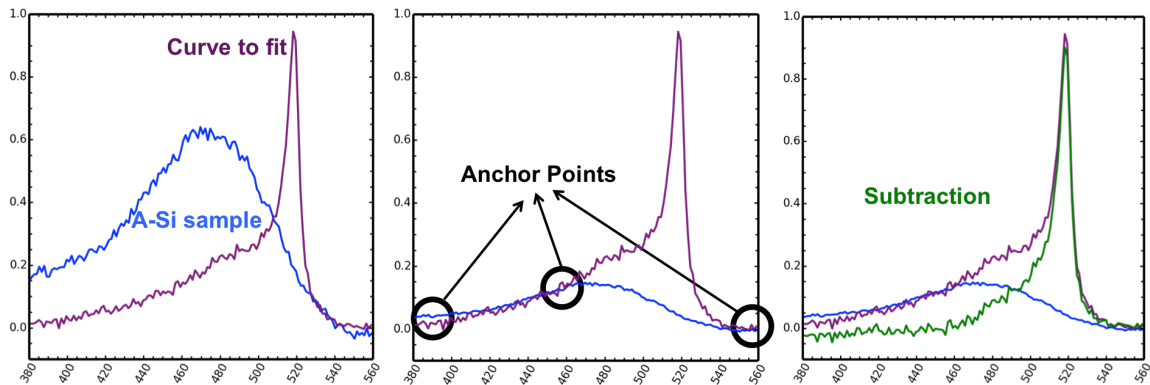
Figure 34- "Subtraction" fitting routine used to determine the crystallinity of SNPs.

Fits using this routine were compared to those obtained using Renishaw's Wire software. The crystallinities achieved using both methods were comparable and were consistent with what could be discerned by examining the curves by eye. All Raman data generated in this work used the methodology described above due to its ability to automate the fitting of multiple samples simultaneously and display visually appealing plots via the matplotlib library for python.

5.2 Calibration
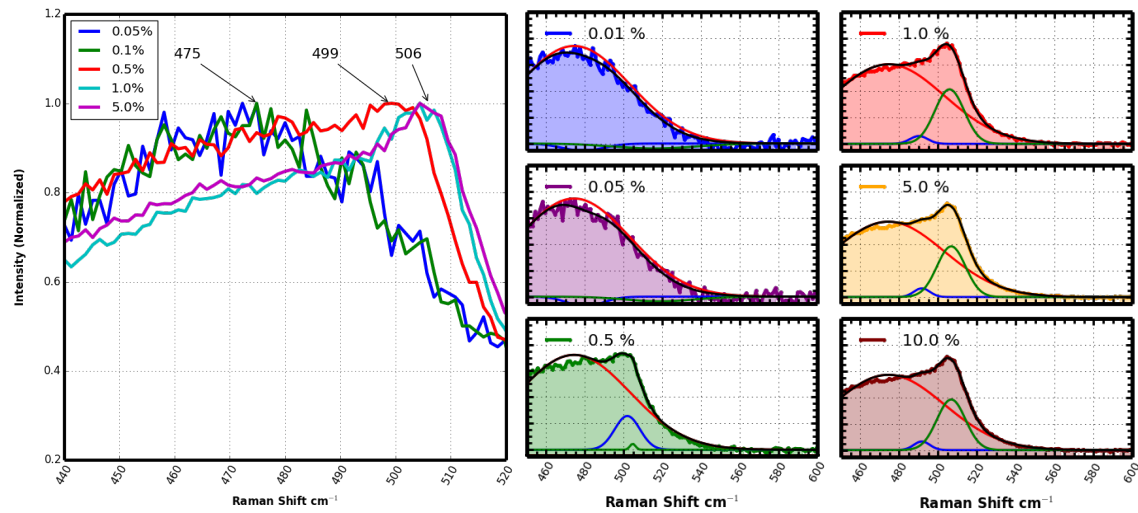
Figure 35 – Effect of laser intensity on the absorption spectra of SNPs. Intensities over 0.05% appear to change the structure of the particle, resulting in erroneous data

One common issue when using Raman spectroscopy to study silicon samples is the potential for the laser to crystallize the sample if its power is set too high. This phenomenon can be observed in Figure 35. In this experiment a sample consisting of known amorphous particles was measured at laser intensities ranging from 0.01% to 10.0% of the maximum intensity. From the chart it can be seen that at low intensities (0.01% and 0.05%) the sample remains unaltered. However, at intensities of 0.5% and above the formation of a peak at approximately 510 cm^{-1} can be seen. Based on this data, all samples analyzed in this work were measured at 0.05% intensity.

6   RESULTS

The experiments that follow had four goals.

1) Evaluate the performance of the plasma chamber (uniformity and process robustness) and use the results to make specific improvements

2) Investigate Deppy's ability to control film and particle properties independently

3) Showcase Deppy's ability to deposit on full sized substrates

4) Contribute to the understanding of SNP synthesis by investigating the influence of chamber conditions on particle morphology

Samples were prepared by depositing thick lines of SNPs onto glass substrates as shown in Figure 36. One parameter (power, pressure or flow rate) was swept from a high value to a low value with each line representing 1 minute of stationary deposition (no chuck translation). This was done to collect enough material to analyze the Raman spectra. For each parameter sweep, the first line was always run at the same conditions (SiH$_4$: 32 sccm, He: 150 sccm, Po: 275, Pressure: 2 Torr) to monitor consistency.
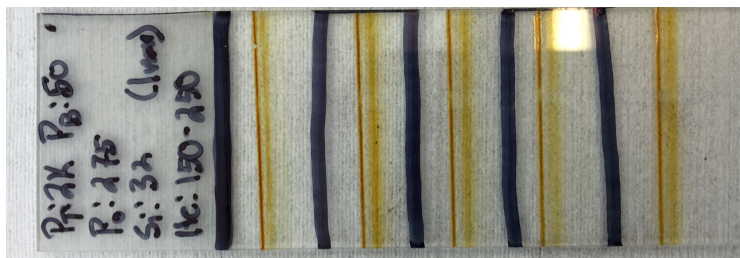
Figure 36 – SNP films deposited at varying process conditions on a glass slide for Raman analysis

A Raman spectra was taken at three points on each line at the following conditions:

Power: 0.05%
Exposer time: 15s
Number of Measurements: 10

6.1 Chamber Comparison
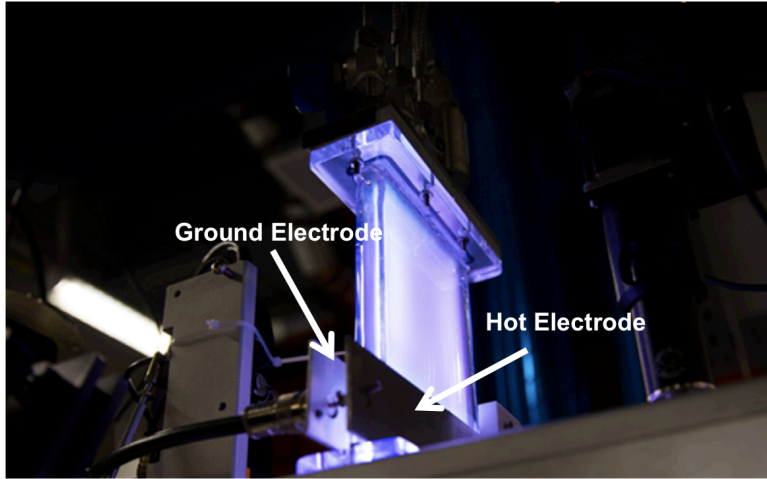
Figure 37 – Deppy equipped with its original capacitively coupled plasma chamber for SNP analysis

Deppy's original synthesis chamber was a quartz tube with electrodes placed on either side to produce a capacitively coupled plasma. An early set of experiments aimed to determine the synthesis capabilities of this setup and give input for the design of the next iteration.

The experiment consisted of synthesizing SNPs at nine different process conditions. For each run power, pressure, and silane flow rate were set to a value of high or low. The conditions for each run are shown in Table 2.

	Power Variation			Silane Variation			Pressure Variation		
	1	2	3	4	5	6	7	8	9
Power (W)	300	200	200	300	300	200	300	300	200
Pressure (mTorr)	1900	1900	1900	1900	1900	1900	1900	2100	2600
Silane (sccm)	15	15	70	15	20	70	15	15	15

Table 2 – Process conditions used for performance comparison of the aluminum and quartz chambers
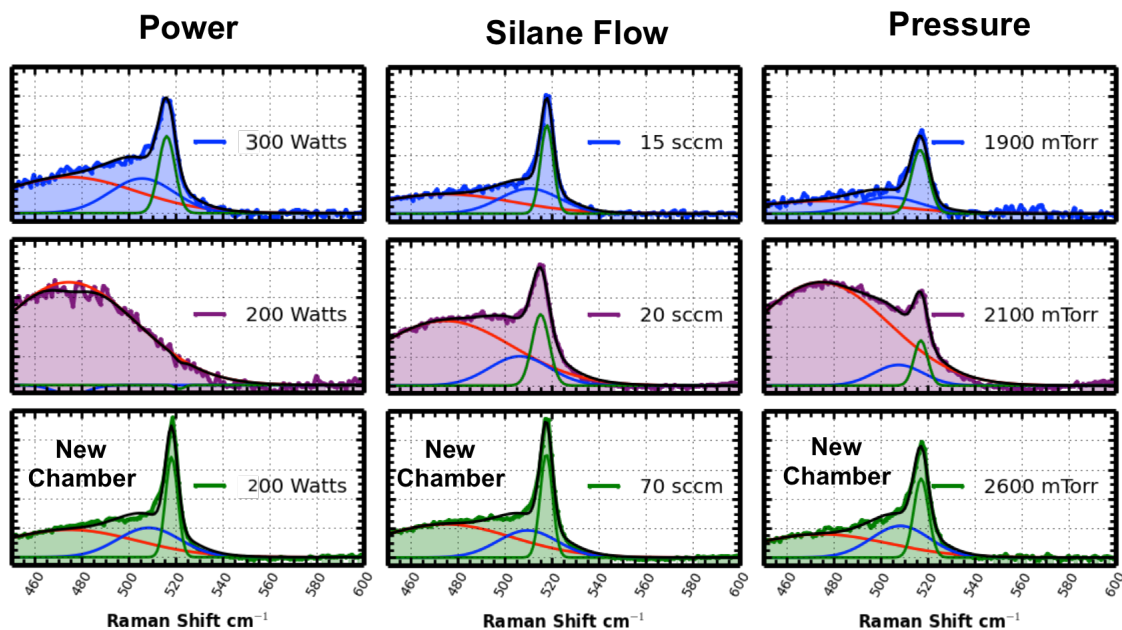
Figure 38 – Raman spectra of particles synthesized in the quartz (blue and purple) and aluminum (green) chambers.

6.1.1 Power

In the first column of Figure 38 the blue curve represents the spectra obtained from sample 1 (S1) and the purple curve from S2. The conditions in Table 2 show that the pressure and silane flow rate were held constant at 1900 mTorr and 15 sccm, respectively, while power was decreased from 300W to 200W. In S1 particles are highly crystalline while at S1 they are completely amorphous. This indicates that the higher the power, the more crystalline the samples will be. Unfortunately, running at 300W with the quartz system was not sustainable long term. Not only did the chamber heat up significantly, so did other system components, in some cases causing damage. Examining the green curve, a sample run under similar conditions in the aluminum chamber, it can be seen that crystalline particles are formed at much lower powers. This implies that power

53

is being more efficiently coupled into the plasma and results in a much cooler running system.

6.1.2 Silane Flowrate

In the second column of Figure 38 the blue curve represents the spectra obtained from S4 and the purple curve from S5. Table II shows that in this sweep, pressure and power were held constant as the silane flow rate was increased. As the flow rate is increased from 15 sccm to 20 sccm the crystallinity decreases. These results are troubling because the transition from amorphous to crystalline occurs at a very low silane flow rate. In most silane PECVD processes the deposition rate is highly dependent on the silane flow rate. To have an industrially competitive rate, Deppy needs to be able to flow significantly more silane and still maintain crystallinity. Sample S1 shows that the aluminum chamber produces highly crystalline particles at flow rates of up to 70 sccm for the same pressure and power. This is a significant improvement attributed to the increased power coupling efficiency.

6.1.3 Pressure

In the third column the chamber pressure was increased from 1900 mTorr (S7) to 2100 mTorr (S8) at constant power and silane flow rate. The data shows a decrease in crystallinity with an increase in pressure. The aluminum chamber once again proves superior, producing crystalline particles at pressures up to 2600 mTorr at the same flow rate and power. This is significant as operating at higher pressures will result in more dense films.

6.2 Influence of Process Variables on Particle Morphology

6.2.1 Helium Flowrate
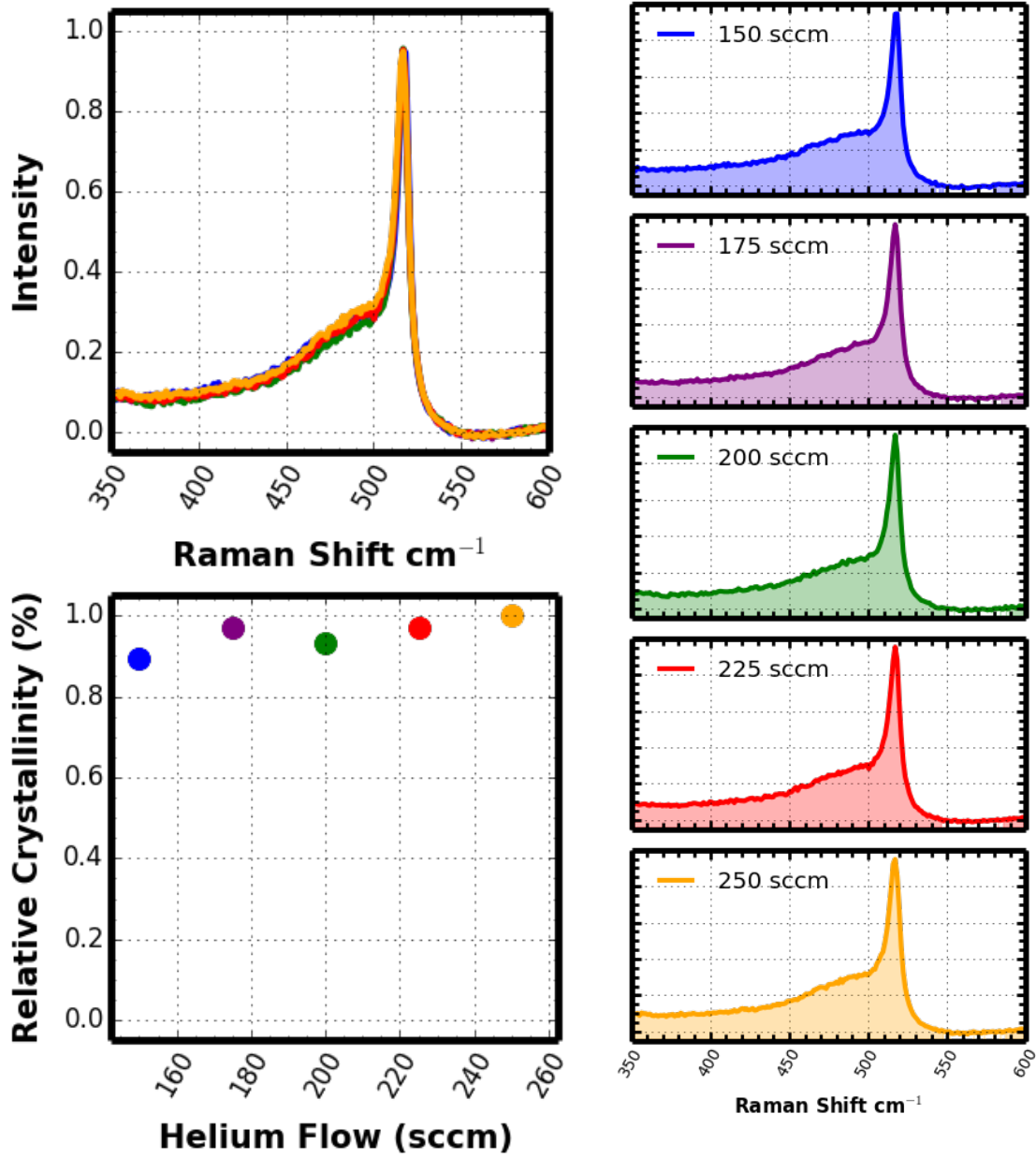
Power (W)	Pressure (mTorr)	Helium Flow (sccm)	Silane Flow (sccm)
275	2000	[150-250]	32

Figure 39 – Raman spectra showing the influence of helium flowrate on crystallinity

In the first set of experiments the helium flow rate was varied from 150 to 250 sccm at the process conditions shown in Figure 39. In order to keep the pressure in the reaction chamber constant with increasing flow, the nozzle width was increased.

The figure shows that the crystallinity of synthesized particles remains fairly constant with increasing helium flow. The lack of a dependence makes the helium flow rate an incredibly useful parameter for adjusting the properties of both the synthesized particles and the deposited films.

The residence time of a particle in a reactor can be defined by the following equation [37]:

Equation 13

$$\tau = \frac{V}{Q}$$

Where:
τ = Residence Time
V = Chamber Volume
Q = Volumetric flow rate

By increasing the helium flow rate at constant pressure, the residence time was decreased from 1.37s to 0.91s. As mentioned earlier in this work, the square root of the residence time has been shown to be proportional to the particle size. With this knowledge the helium flow rate can be used to change the residence time and particle size while keeping a constant particle structure.

Increasing the helium flow rate also allows for an increase in nozzle width while maintaining constant pressure. That means the helium flow rate can be used to indirectly adjust the impact velocity. Increasing the nozzle width also benefits the film uniformity by reducing particle buildup as will be discussed in a later section.

56

6.2.2 Silane Flow Rate
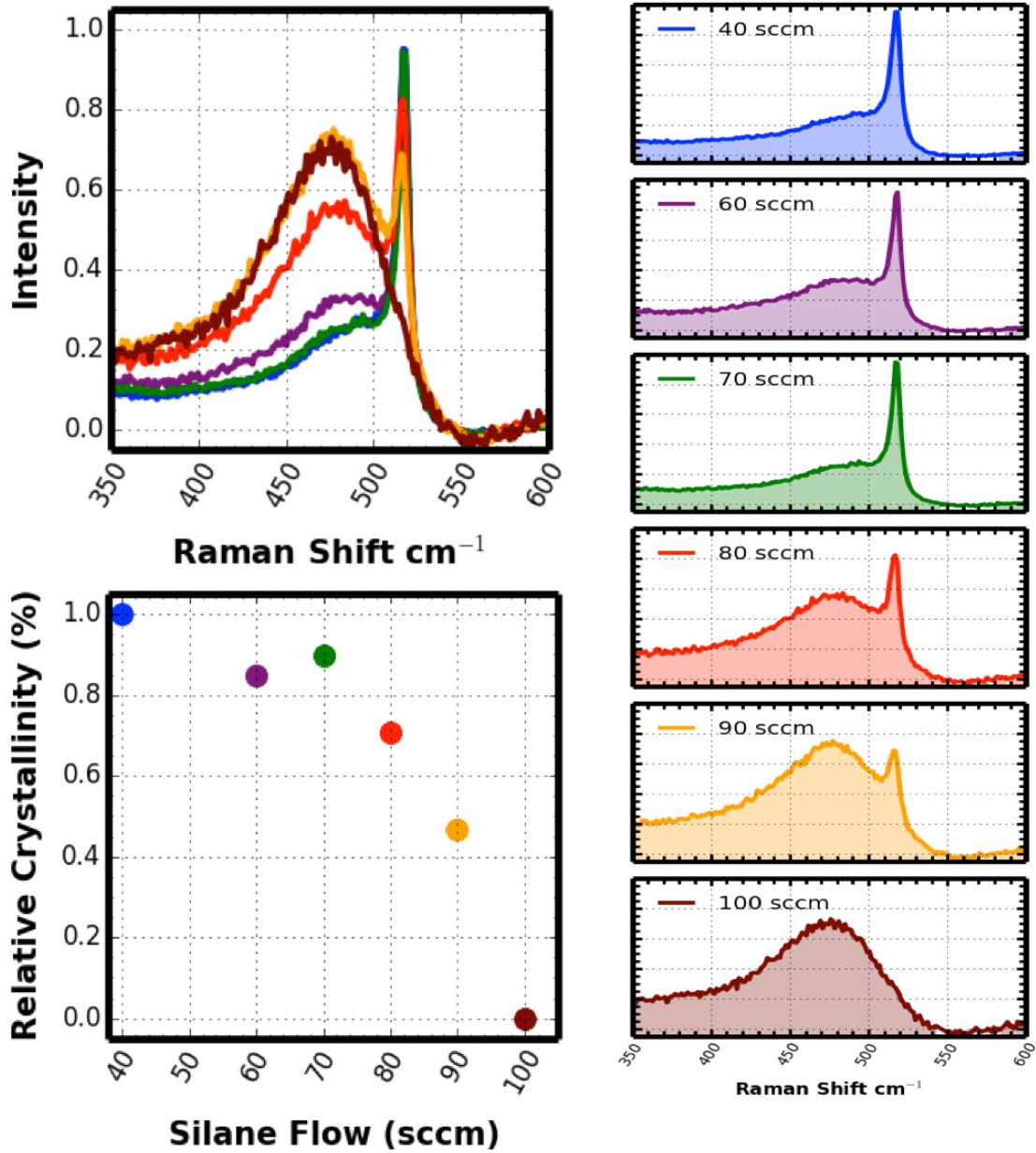
Power (W)	Pressure (mTorr)	Helium Flow (sccm)	Silane Flow (sccm)
275	2000	150	[40-100]

Figure 40 - Raman spectra showing the influence of silane flowrate on crystallinity

In this set of experiments the silane flow rate was varied from 40 sccm to 100 sccm at the conditions shown in Figure 40. To keep the pressure in the reaction chamber constant with the increasing gas flow the nozzle width was increased.

Increasing the silane flow rate has the eventual effect of decreasing the crystallinity of the particles. The chart above indicates that the crystallinity remains relatively constant until ~ 80sccm, after which the crystallinity declines rapidly. The data indicates a range of silane flow rates where crystallinity is high and relatively constant. This range is bounded on the high end by a minimum silane flow rate to applied power ratio that will yield crystalline particles.

As the flow rate is decreased further into the crystallization zone an interesting phenomenon occurs: deposition ceases entirely. The picture below shows the glass slide used to collect the particles produced during the deposition. Each orange line represents a silane flow rate starting with 40 sccm being the line on the far left.
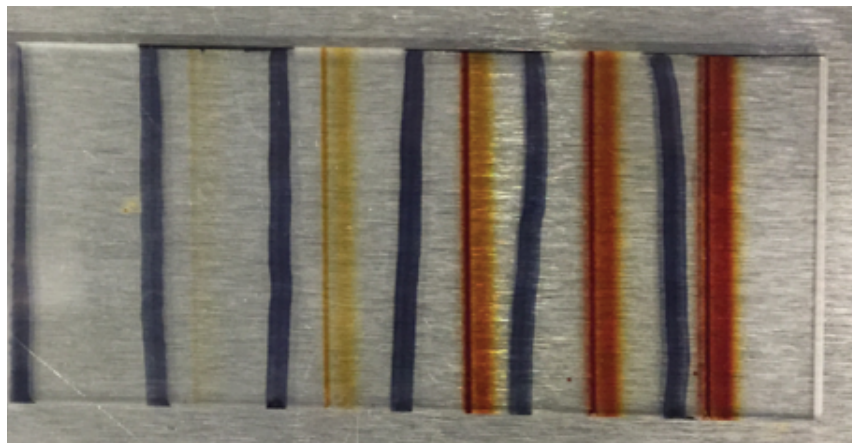
Figure 41 – Nanoparticles deposited on a glass slide during a RF power sweep. As power increased the amount of deposition decreased significantly

Limited deposition would not be so surprising as the silane flow rate decreases if we had not observed a significant amount at 15 sccm and 200W in the experiments de-

scribed in Figure 38. A number of groups have observed that at larger power to flow ratios SNPs are formed just as quickly as they are dissociated by atomic collisions, resulting in a near zero deposition rate. This presents an interesting challenge for plasma- based synthesis. A minimum power is required to crystallize particles, but too much results in no particle formation at all.

6.2.3 Power
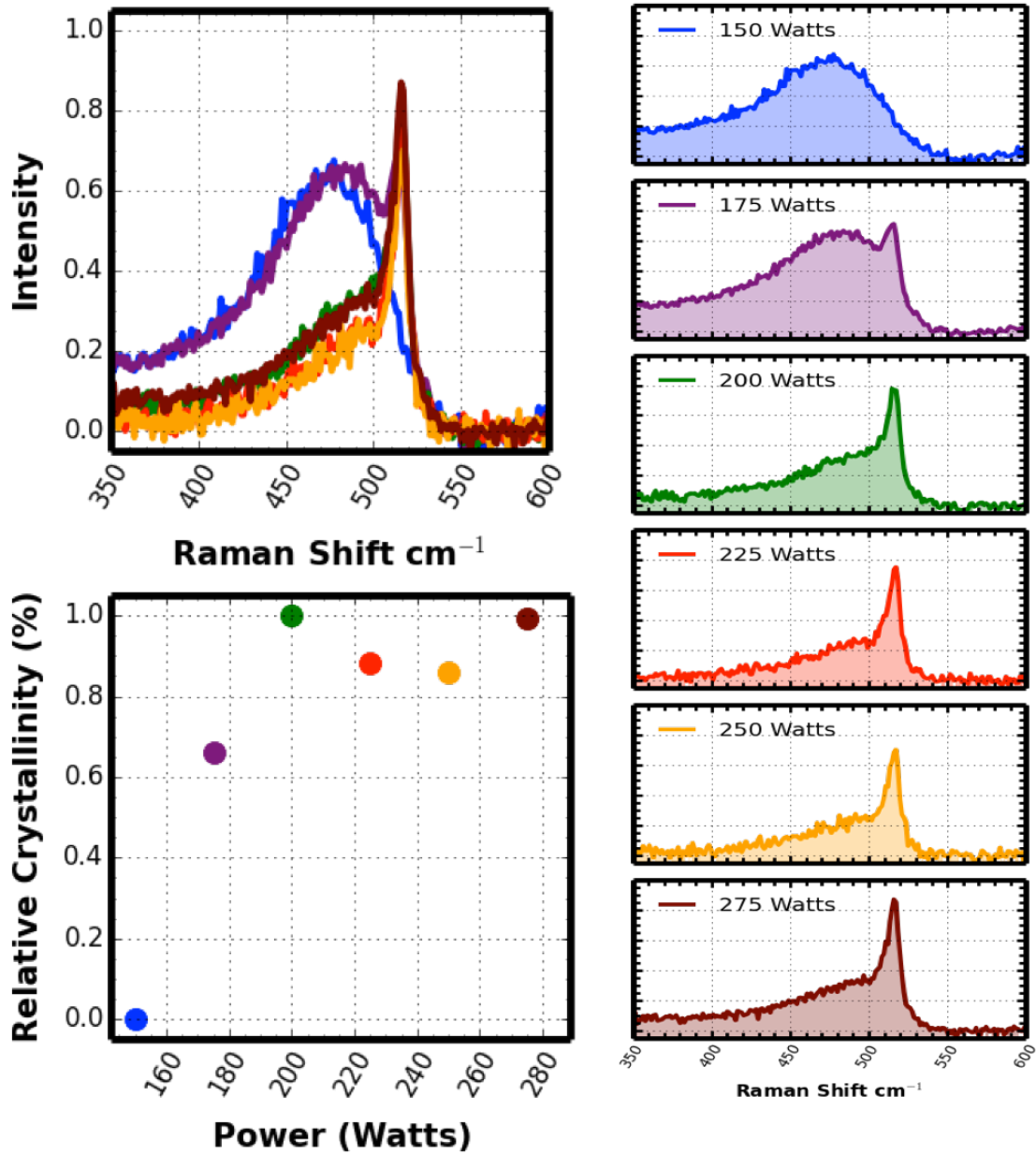
Power (W)	Pressure (mTorr)	Helium Flow (sccm)	Silane Flow (sccm)
[150-275]	2000	150	32

Figure 42 - Raman spectra showing the influence of RF power on particle crystallinity

In this set of experiments the power was varied from 150W to 275W at the conditions shown in the table in Figure 42. The figure above shows that crystallinity increases with increasing power. This is expected as more energy is supplied to aid in crystallization. From Figure 42 it can be seen that above a minimum power, particle crystallinity remains fairly constant. Below this minimum power crystallinity rapidly decreases with applied power. This is further evidence for the existence of a minimum silane flow to power ratio that results in crystalline particles.

6.2.4 Pressure
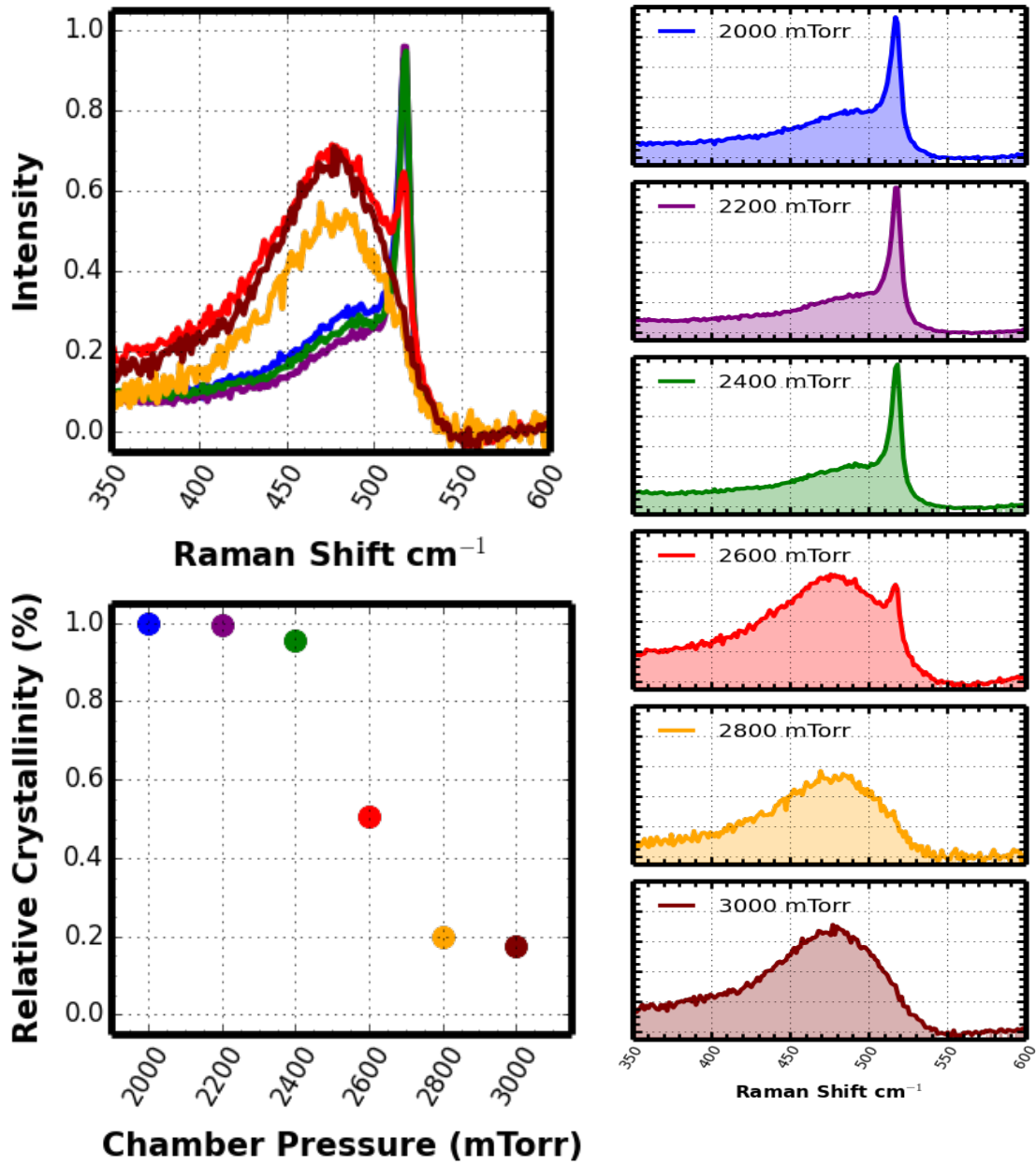
Power (W)	Pressure (mTorr)	Helium Flow (sccm)	Silane Flow (sccm)
275	[2000-3000]	150	32

Figure 43 - Raman spectra showing the influence of pressure on particle crystallinity

In this sweep, pressure was varied from 2000mTorr to 3000mTorr at constant power and silane flow rate by adjusting the width of the nozzle. The data shows that as pressure increases, crystallinity decreases. Figure 43 shows that above a maximum pressure the crystallinity begins to decrease rapidly while it remains relatively constant below said pressure. This further supports the claim that a minimum silane to power ratio is required for crystalline particle formation. Increasing the pressure increases the amount of silane in the chamber at any moment in time, in affect decreasing the ratio.

The maximum pressure for crystalline particles results in a maximum pressure ratio which determines the maximum film density. In order to run at higher pressures and deposit ultra-dense films, more power will need to be applied.

6.2.5 Deposition Optimization

Armed with a thorough understanding of how process parameters affect particle synthesis, attention can be turned to film deposition. Deppy's ability to deposit nanoparticles on substrates up to 100mm in diameter make it the first of its kind. Like all systems that aim to deposit films over large areas, uniformity is a primary concern. Deppy's unique design brings with it a number of unique challenges that will need to be addressed for the tool to be considered industrially viable.
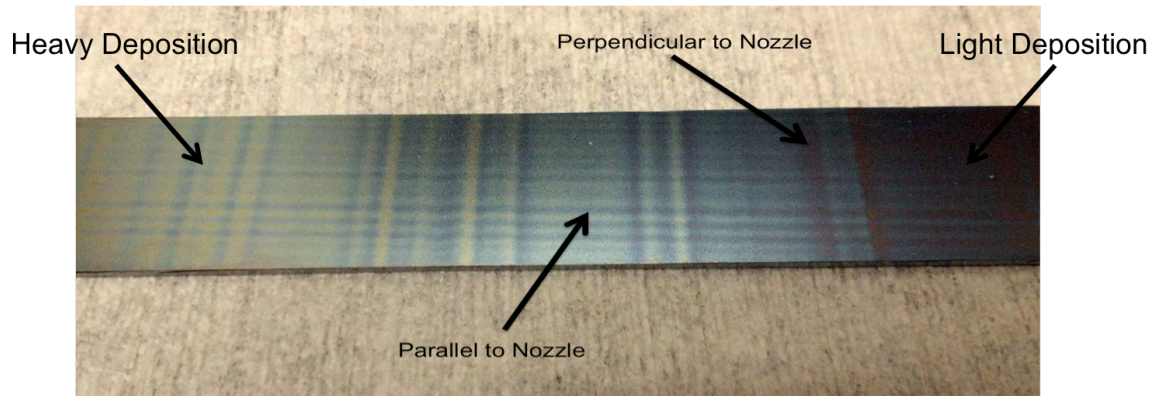
Figure 44 – Silicon substrate that has been put through a SNP deposition process. The substrate displaces a number of different non-uniformities

Figure 44 is a slice of a 100mm substrate with a SNP film deposited by Deppy. As the text indicates, its long edge was parallel to the nozzle during deposition. This figure indicates three separate problems with Deppy's deposition process.

1) Regularly spaced lines of varying film thickness that run parallel to the nozzle and perpendicular to the direction of movement

2) Irregularly spaced lines perpendicular to the nozzle, parallel to the direction of movement

3) A thickness variation across the sample

The regular spacing of the lines parallel to the direction of movement indicated that the issue might be tied to the stepper motor that controls the chuck's motion. Upon further investigation we found that if the speed at which the chuck passes underneath the nozzle is increased, one set of lines disappears as shown in Figure 45.
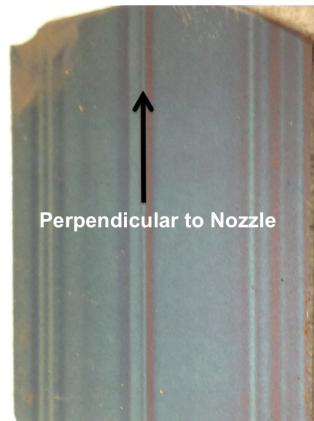
Figure 45 – Silicon sample deposited with increased chuck speed removed the regularly spaced non-uniformities from the film.

Visually observing the chuck's motion, we could see that at low speeds (<100 mm/s) the chuck "stuttered" with each step of the stepper motor. This was not as apparent at high speeds. Since the final thickness of the film is determined in part by the speed at which the substrate passes beneath the nozzle, depositing very thick films can only be accomplished by increasing the number of passes.

The magnitude of this problem and the effectiveness of this solution are up for debate. The applications that we are currently targeting require very thin films (<100 nm), for which the use of a high chuck velocity is advantageous. As of yet, no applications for films thick enough to warrant a slower speed are being investigated, but in the interest of our tool's robustness this problem will certainly need to be addressed in the future.

The irregular spacing of the lines parallel to the direction of motion and perpendicular to the nozzle indicate a blockage in the path of the jet stream containing the nanoparticles. Indeed we found upon examining the nozzle that agglomerates of particles had become stuck in the nozzle impeding gas flow as shown in Figure 46.
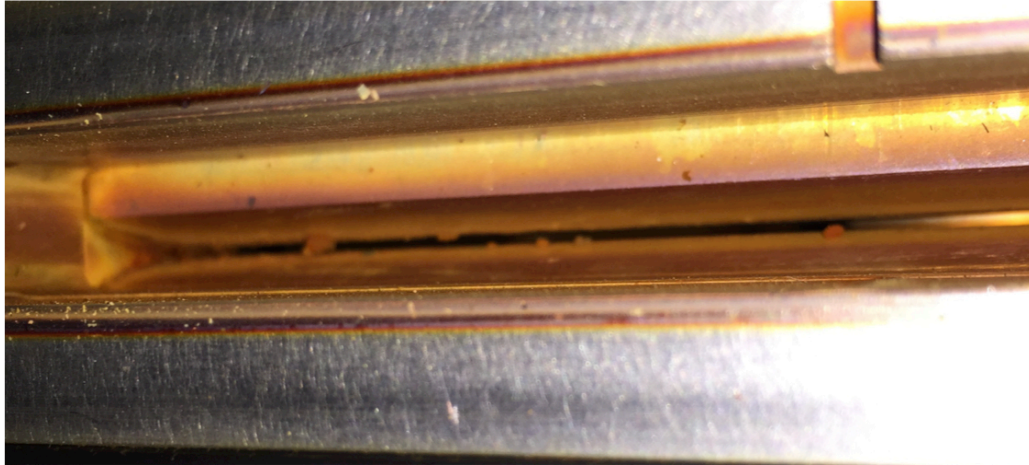
Figure 46 – Top view of the nozzle after several hours of deposition. Large particle can be seen trapped in the fluid flow path

Cleaning the nozzle with a cleanroom cloth and IPA removed the lines resulting in the smooth film in Figure 47 below.

Figure 47 – Sample deposited at a high chuck speed after a nozzle clean

The nozzle clogging presents a significant barrier towards the industrialization of this tool. The conditions under which the previous four figures were created allowed for approximately 2 hours of deposition before the nozzle required cleaning. Increasing the nozzle width (keeping the pressure constant by increasing the helium flowrate) did in-

crease the time between cleanings to over an hour. This method does however limit our ability to control the residence time and particle size.

As this project moves forward, solving the issue of nozzle clogging is of critical importance. An industrial tool should be able to operate for hundreds of hours without a manual clean. Possible solutions include a plasma clean (NF_3) at regular intervals.

The final challenge deals with the non-uniformity across the length of the wafer. In some cases this can be disastrous. As shown in Figure 48, very heavy deposition occurs on the one side of the chuck (this side will be referred to as the Window Side) and nearly no deposition occurred on the other (baratron side).
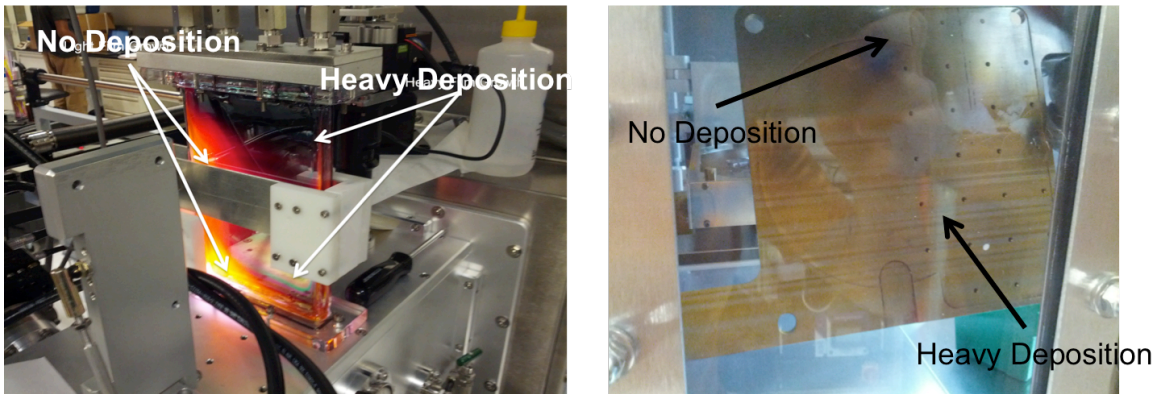
Figure 48- Non-uniform deposition visible after several runs

Over the course of this work it was found that this extreme non-uniformity can be attributed to several design related issues. The first issue is gas mixing. In the set-up that was used to produce Figure 48, the silane gas was introduced on the window side of the chamber (the side with the heavy deposition in Figure 48). Switching the silane gas inlet to the center position on the showerhead resulted in a significant uniformity improvement as shown in Figure 49.
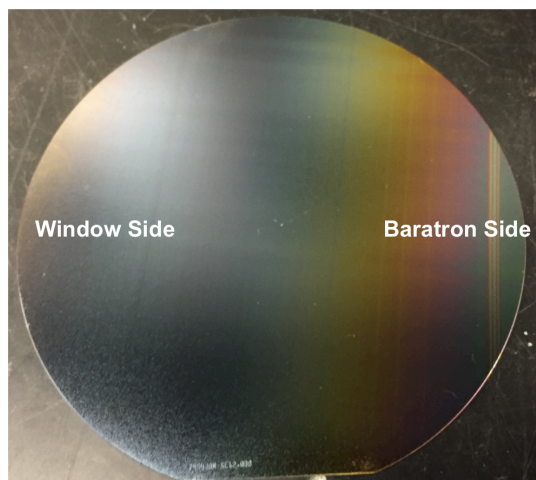
Figure 49 – 100mm silicon wafer deposited with film of SNP. The color variation indicates significant differences in film thickness between the left and right sides

Even after switching the gas inlet, a thickness gradient still existed in the chamber, though interestingly the pattern had reversed! In a serendipitous discovery it was found that the baratron measuring the pressure in the reaction chamber was having a significant influence on the uniformity. Figure 50 below shows the film deposition on the electrodes with (top) and without (bottom) the baratron plugged into its power source. When the baratron is plugged in, deposition heavily favors the baratron side and when it is unplugged a much more uniform film is deposited.
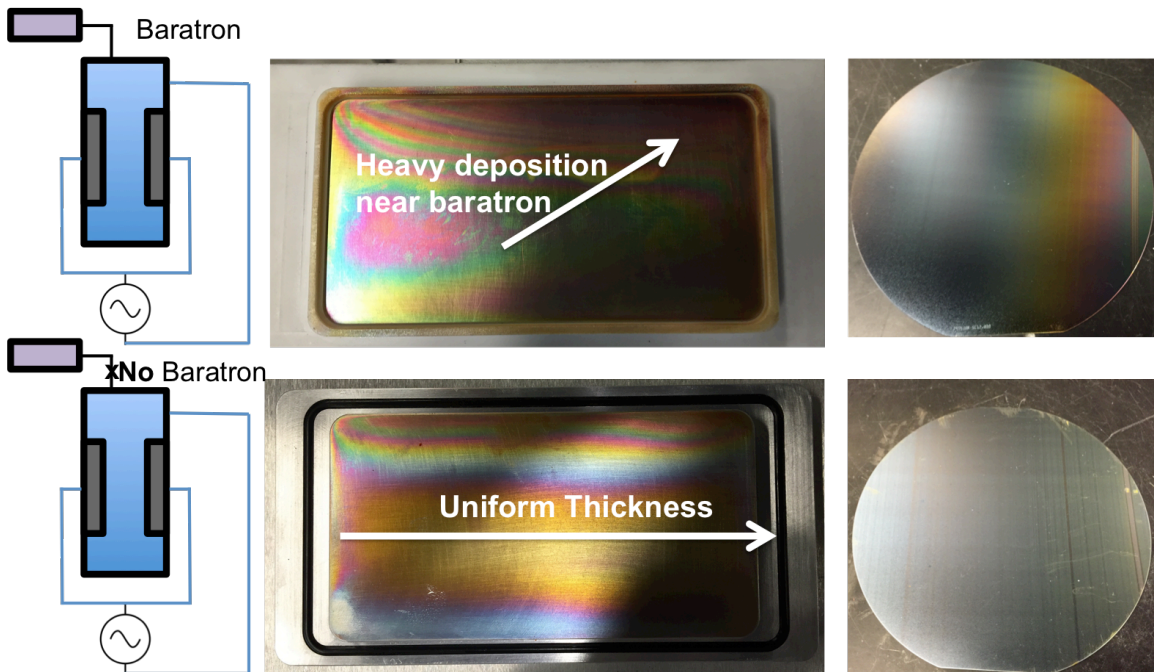
Figure 50 – Effect of removing power to the baratron. Without the baratron plugged in, uniformity improves significantly

The process is being run without the baratron plugged in. This is a temporary solution as the ability to monitor the pressure in the reaction chamber during the process is lost.

6.2.6 Chamber Heating

Another issue encountered while studying the properties of the deposited films was the effect of chamber heating on the synthesis process. The samples in Figure 51 were run at the same conditions ~24 minutes apart with several other samples run in between.
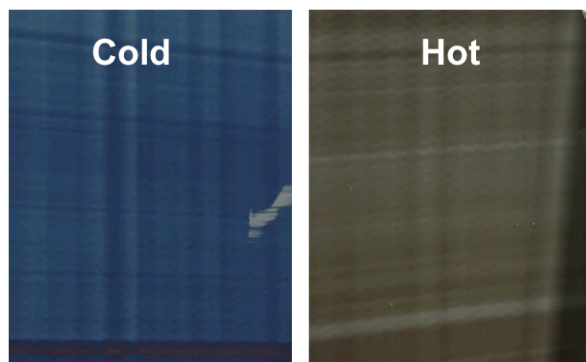
Figure 51 – Variation in film thickness for the same deposition conditions run 24 minutes apart. This variation is attributed to chamber heating.

SEM analysis showed that the deposition rate of the blue sample was 2.5x larger than that of the brown sample (50nm/pass vs. 21 nm/pass). Further investigation revealed that this decrease in deposition rate could be attributed to an increase in the chamber temperature. After 24 minutes the chamber temperature was measured to be ~ 90^{0}C. Up-on letting the chamber cool down deposition returned to normal.

As with most silane based deposition processes, the deposition rate is highly de-pendent on the silane flow rate. From the data observed in this work thus far, we can safely say that in order to produce crystalline SNPs for a high rate process a high RF power generator will need be used. The effect of chamber heating on the deposition rate however adds another barrier. The rate that the chamber heats up will be proportional to the applied power. In order to run a high-powered process and keep the chamber cool a modified chamber with water-cooling will need to be designed.

6.2.7 Film Density

A key feature of HPD is the ability to significantly vary the density of deposited films. This is something that is largely not possible with standard plasma or thermal dep-

osition techniques. In this tool, density can be varied in three ways: changing the pressure ratio, varying the nozzle width, and varying the distance from the nozzle to the chuck.

For this initial set of experiments the nozzle was kept at a constant width, the chuck kept at a constant distance of 30mm from the nozzle, the RxC chamber pressure was kept at 2000mTorr and the DpC pressure was varied to produce pressure ratios of 40, 10 and 5. Samples were swiped beneath the nozzle 100 times at 100 mm/s. From the analysis in the Theory of Operation section of this work it was determined that at these conditions impact velocity would be 1025 m/s, 825 m/s and 550 m/s for pressure ratios of 40, 10 and 5, respectively. For each of the samples SEM analysis was conducted using a Philips XL30.

160 nm   700 nm   270 nm

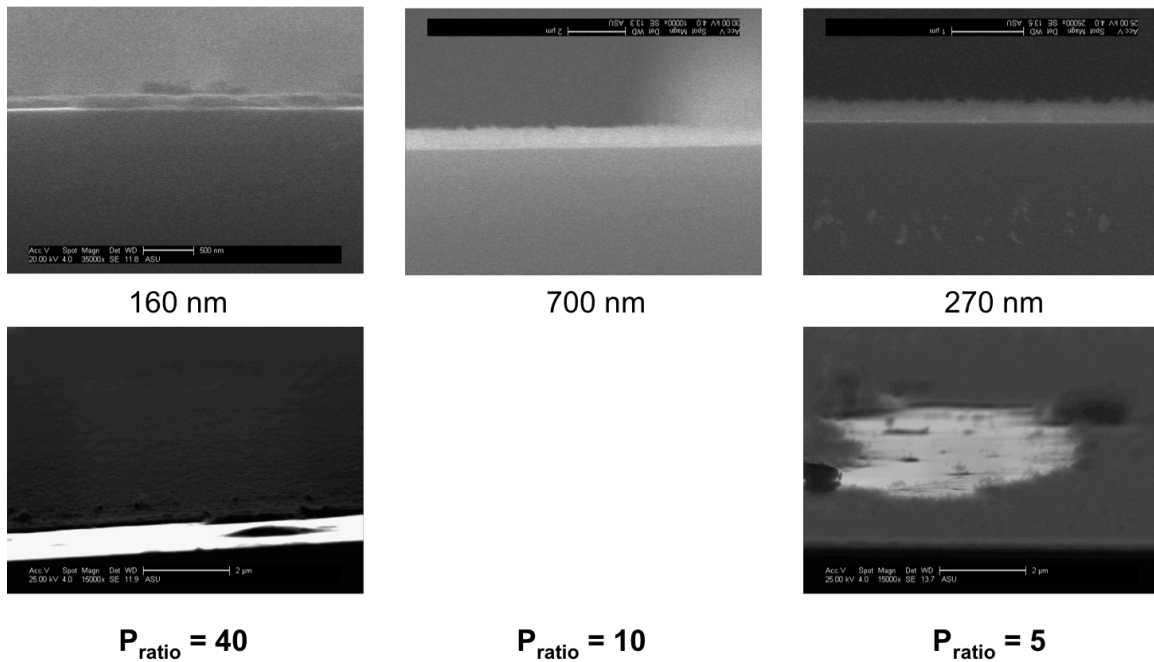P_{ratio} = 40 P_{ratio} = 10 P_{ratio} = 5

Figure 52- SEM images of SNP films deposited at varying pressure ratios

Figure 52 shows the significant impact that pressure ratio has on the final film density. Looking at the aerial shots of the films it is clear that at lower pressure ratios

71

films become less dense and more "fluffy." An unexpected result is the decrease in film thickness from the second to third sample. One would expect that at the lower pressure ratio, the film would be less dense and thus thicker than a film deposited at a higher ratio, a relationship that indeed holds true between the first and second samples.

Revisiting Figure 18, it can be seen that the velocity of the of particles at the 5x pressure differential is about two-thirds the velocity of the 10x simulation and one-half that of the 40x simulation. What Figure 18 fails to show is the direction of the particles velocity. The vacuum pump pulls particles in a direction perpendicular to that of the jet stream. If a particle's vertical velocity (in the direction of the substrate) is not large enough, the horizontal component will direct the particle away from the substrate, completely avoiding an impaction event. This is especially true for small particles. Referencing Equation 10, the drag force of a particle located in the jet stream is proportional to the square of the diameter. Smaller particles will experience much lower vertical velocities than their larger counterparts and be more likely to miss the substrate. Simply put, while the 5x deposition is less dense than the 10x and 40x, significantly less material reaches the substrate resulting in a thinner film.

The primary goal of this work is to prove that Deppy is capable of varying particle synthesis and film properties independently. Figure 3 shows the Raman spectra for each of the samples above. The spectra remain relatively constant in spite of the drastic pressure differential changes.
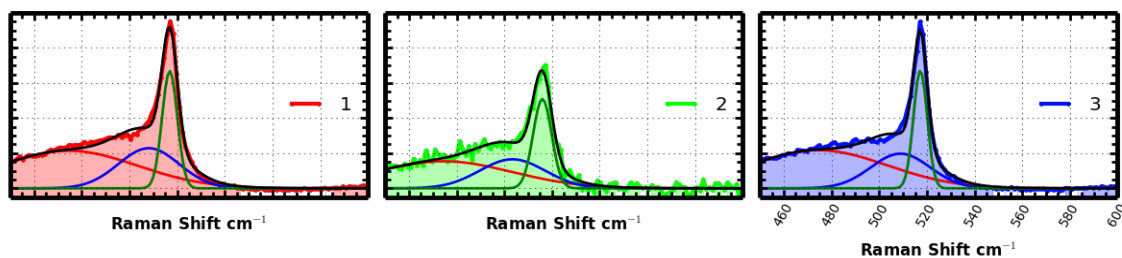
Figure 53 – Raman spectra for the films deposited in Figure 52. The spectra remain relatively constant in spite of drastic changes in density.

6.2.8 Uniform Deposition onto 3D Objects

One of Deppy's more unique features is the ability to deposit uniform nanoparticle films onto 3D objects. From a theoretical standpoint, the density and thickness of a film deposited on a 3D object should remain constant so long as the impact velocity at each point along the object is constant. Deppy can accomplish this by varying the pressure ratio or the distance from nozzle to object in accordance with the objects topography. Figure 54 shows a relatively uniform coating deposited on a 3D object (golf ball) using a rudimentary height mapping routine. Future work will improve upon this routine expanding Deppy's software to handle the coating of arbitrarily shaped objects.

Figure 54 – Uniform deposition over the top hemisphere of a golf ball; proving Deppy's ability to coat uniquely shaped and nontraditional objects.

7 FUTURE AND ONGOING WORK

In this work the feasibility of hypersonic particle deposition as a method for large-scale nanomaterial deposition was investigated. A custom large-scale HPD system was designed to accomplish this goal. A significant percentage of the initial effort in this project was dedicated to the setup, automation, and fine-tuning of the design. The initial results are promising and indicate that the system meets the three critical criteria to justify moving forward.

1) Ability to control particle properties

Current Status:

By adjusting the conditions in the RxC the particle morphology of silicon nanoparticles was varied from completely amorphous to highly crystalline. The data collected using the initial quartz chamber shed light onto the inefficiencies of several of Deppy's components. Addressing these issues and modifying the tool allowed for the collection of data concerning the influence of power, pressure, and silane flow rate on the synthesis of silicon nanoparticles via non-thermal plasma.

Future Work:

Another important consideration when synthesizing nanoparticles is the size and size distribution of the particles. In plasma synthesis, the average size is determined by the residence time in the chamber, with longer residence times resulting in larger particles. Using TEM microscopy Deppy's ability to control particle size by adjusting the residence time will be investigated.

2) Ability to control film properties

Current Status:

The densities of films were seen to change when deposited at varying pressure ratios, with higher-pressure ratios resulting in visually denser films than the low ratio films. Raman spectroscopy showed that varying the film density did not have an influence on particle crystallinity.

Future Work:

The relationship between pressure ratio, total gas flow, and particle composition will be further investigated using Rutherford Backscattering and ellipsometry. Ideally an analytical model for film densities deposited via HPD applicable to a wide range of materials will be developed. Development of the model is a critical step in the commercialization of the tool.

3) Substrate Independence

Current Status:

Throughout this work it was shown that Deppy is capable of depositing nanoparticles on multiple types of materials including silicon wafers, glass, plastics, aluminum and 3D objects.

Future Work:

Future work will involve identifying industrially valuable nanoparticle/substrate pairs that are not efficiently produced using current methods. This will require the purchase of an aerosolization machine so that focus can be put on integrating the HPD technology with varying synthesis techniques.

Further work will be done improving Deppy's ability to coat arbitrarily shaped 3D objects by integrating software capable of translating the topography of the objects to variation of the chuck's movement and chamber conditions.

A summary of Deppy's capabilities compared to those of other synthesis and deposition methods is shown in Table 3 below.

Synthesis Method	Continuous Processing	Particle Independent	Substrate Independent	Film Density Control	Coat 3D Objects
Pyrolysis	✓	✗	✗	✗	✗
Solution Methods	✗	✗	✗	✓	✓
Plasma	✓	✓	✗	✗	✗
Deppy (HPD)	✓	✓	✓	✓	✓

Table 3 – Summary of nanomaterial synthesis methods and their abilities

WORKS CITED

[1] K. A. Littau and P J Szajowski, "Luminescent Silicon Nanocrystal Colloid via a High-Temperature Aerosol Reaction," The Journal of Physical Chemistry, vol. 97, no. 6, pp. 1224-1230, 1993.

[2] C Hollenstein and A. A. Howling, "Dust Particle Diagnostics in RF Plasma Deposition of Silicon and Silicon Oxide Films," MRS Proceedings, vol. 507, 1998.

[3] Tae Wook Kim and Chang-Hee Cho, "Quantum confinement effect in crystalline silicon quantum dots in silicon nitride grown using SiH4 and NH3," APPLIED PHYSICS LETTERS, vol. 88, March 2006.

[4] Lorenzo Pavesi and Turan Rasit, Silicon Nanocrystals.: WILEY-VCH Verlag GmbH & Co. , 2010.

[5] X D Pi and Eneen J Nowak, "Air-stable full-visible-spectrum emission from silicon nanocrystals synthesized by an all-gas-phase plasma approach," Nanotechnology, vol. 19, no. 24, 2008.

[6] Matthew C Beard and Kelly P Knutsen, "Multiple Exciton Generation in Colloidal Silicon Nanocrystals," Nano Letters, vol. 7, no. 8, pp. 2506-2512, 2007.

[7] Andres Cuevas, "The effect of emitter recombination on the effective lifetime of silicon wafers," Solar Energy Materials and Solar Cells, 1999.

[8] L Mangolini and U Kortshagen, "Plasma-Assisted Synthesis of Silicon Nanocrystal Inks," Advanced Materials, 2007.

[9] DuPont. (2012) DuPont Innovalight Selective Emitter Platform: Raising the Efficiency of Solar Cells. [Online]. http://www.dupont.com/products-and-services/solar-photovoltaic-materials/articles/innovalight-selective-emitter-platform.html

[10] Christiana Honsberg and Stuart Bowden. (2013) PV Education. [Online]. http://www.pveducation.org/pvcdrom/design/anti-reflection-coatings

[11] Atul Madhavan. (2009) Alternative designs for nanocrystalline silicon solar cells (Doctoral dissertation).

[12] E Vallat-Sauvain and J Bailat, "Influence of the substrate's surface morphology and chemical nature," Thin Solid Films, 2005.

[13] Kim Taekon. (2009) CRYSTALLIZATION OF AMORPHOUS SILICON THIN FILMS INDUCED BY NANOPARTICLE SEEDS (Doctoral Dissertation).

[14] Platinum Price. (2015) Platinum Price Per Ounce. [Online].
http://platinumprice.org/platinum-price-per-ounce.html

[15] NY Daily News. (2014, Jan) Daily News - Autos. [Online].
http://www.nydailynews.com/autos/auto-sales-reach-six-year-high-demand-peaked-article-1.1567645

[16] Markus Nesselberger and Melanie Roefzaad, "The effect of particle proximity on the oxygen reduction rate of size-selected platinum clusters," Nature Materials, vol. 12, July 2013.

[17] Gyo Koo and Myoung Lee, "Platinum nanoparticles prepared by a plasma-chemical reduction method," Journal of Materials Chemistry, vol. 15, pp. 4125–4128, August 2005.

[18] Michele L Ostraat and Jan W. De Blauwe, Ultraclean Two-Stage Aerosol Reactor for Production of Oxide-Passivated Silicon Nanoparticles for Novel Memory Devices.: Journal of The Electrochemical Society , 2001, vol. 148.

[19] Z C Holman and U R Kortchagen, "Plasma production of nanodevice-grade semi-conductor nanocrystals ," JOURNAL OF PHYSICS D: APPLIED PHYSICS , vol. 44, 2011.

[20] MARKUS NIEDERBERGER, "Nonaqueous Sol–Gel Routes to Metal Oxide Nano-particles," Acc. Chem. Res., vol. 40, pp. 793–800, 2007.

[21] Larry L Hench and Jon K West, "The Sol-Gel Process," Chem. Rev., pp. 33-72, 1990.

[22] Victor I Klimov, Nanocrytal Quantum dots, 2nd ed.: CRC Press.

[23] C B Murray and D J Norris, "Synthesis and Characterization of Nearly Mono-dispersed CdE (E = S, Se, Te) Semiconductor Nanocrystallites," J. Am. Chem. Soc, vol. 115, pp. 8706-8715 , 1993.

[24] Uwe Kortshagen , "Nonthermal plasma synthesis of semiconductor nanocrystals," J. Phys. D: Appl. Phys. , 2009.

[25] Z C Holman and U R Kortshagen, "A flexible method for depositing dense nano-crystal thin films: impaction of germanium nanocrystals ," Nanotechnology , July 2010.

[26] C R Gorla and S Liang, "Silicon and germanium nanoparticle formation in an induc-tively coupled plasma reactor," J. Vac. Sci. Technol., 1997.

[27] Toru Ifuku and Masanori Otobe, "Fabrication of Nanocrystalline Silicon with Small Spread of Particle Size by Pulsed Gas Plasma ," Jpn. J. Appl. Phys, vol. 36, 1997.

[28] N P Rao and H J Lee, "NANOSTRUCTURED MATERIALS PRODUCTION BY HYPERSONIC PLASMA PARTICLE DEPOSITION," NanoStructured Materials, vol. 9, 1997.

[29] James O Wilkes, Fluid Mechanics for Chemical Engineers.: Prentice Hall.

[30] L D Landau and E M Lifshitz, Fluid Mechanics, Second Edition ed.: Pergamon, 1987.

[31] J M Smith, H C Van Ness, and M M Abbott, Introduction to Chemical Engineering Thermodynamics.: McGraw-Hill.

[32] B Launtrup, Physics of Continuous Matter, Second Edition ed.: CRC Press, 2011.

[33] Michael Lieberman and Allan Lichtenberg, Principles of Plasma Discharges and Materials Processing, 2nd ed.: Wiley.

[34] N Vaghela. Application Note - RF (13.56MHz) Impedance Matching. [Online]. https://chasqueweb.ufrgs.br/~ckrug/pvd/rf-1.pdf

[35] H K Yue and D Li, "ANALYSIS AND DESIGN OF THE MATCHING UNIT FOR AN RF DRIVEN PLASMA SOURCE FOR FUSION PURPOSE," Proceedings of IPAC2013, Shanghai, China.

[36] Corinne Droz, "PhD Thesis: Thin Film Microcrystalline Silicon Layers and Solar Cells," University of Neuchtel, 2003.

[37] Scott Fogler, Elements of Chemical Reaction Engineering.: Prentice-Hall, 1986.

[38] Ellen Fynan and Robert Webster, "DNA Vaccines: Protective Immunizations by Parenatal, Mucosal, and Gene-Gun Injections," Immunology, 1993.

[39] R S Lima and B R Marple, "Thermal Spray Coatings Engineered from Nanostruc-tured Ceramic Agglomerated Powders for Structural, Thermal Barrier and Biomedical Applications: A review," Journal of Thermal Spray Technology, 2007.

[40] Valentin Todorow. (2009, December) Impedance Matching and Matching Networks. [Online]. http://www.engr.sjsu.edu/rkwok/Engr297/Val_Impedance%20Matching%20and%20Matching%20Networks.pdf

[41] R J Shul and J S Pearton, Handbook of Advanced Plasma Processing Techniques.: Spring